



LAWRENCE  
LIVERMORE  
NATIONAL  
LABORATORY

# Numerical Methods for Radiation Magnetohydrodynamics in Astrophysics

R. I. Klein, J. M. Stone

November 28, 2007

Structure Formation in the Universe  
Chamonix, France  
May 27, 2007 through June 2, 2007

## **Disclaimer**

---

This document was prepared as an account of work sponsored by an agency of the United States government. Neither the United States government nor Lawrence Livermore National Security, LLC, nor any of their employees makes any warranty, expressed or implied, or assumes any legal liability or responsibility for the accuracy, completeness, or usefulness of any information, apparatus, product, or process disclosed, or represents that its use would not infringe privately owned rights. Reference herein to any specific commercial product, process, or service by trade name, trademark, manufacturer, or otherwise does not necessarily constitute or imply its endorsement, recommendation, or favoring by the United States government or Lawrence Livermore National Security, LLC. The views and opinions of authors expressed herein do not necessarily state or reflect those of the United States government or Lawrence Livermore National Security, LLC, and shall not be used for advertising or product endorsement purposes.

# Numerical Methods for Radiation Magnetohydrodynamics in Astrophysics

By RICHARD I. KLEIN<sup>1</sup> AND JAMES M. STONE<sup>2</sup>

<sup>1</sup>Department of Astronomy, University of California, Berkeley, Berkeley, CA 94720, and Lawrence Livermore National Laboratory, P.O. Box 808, L-23, Livermore, CA 94550

<sup>2</sup>Department of Astrophysical Sciences, Princeton University, Princeton, NJ 08540, USA

We describe numerical methods for solving the equations of radiation magnetohydrodynamics (MHD) for astrophysical fluid flow. Such methods are essential for the investigation of the time-dependent and multidimensional dynamics of a variety of astrophysical systems, although our particular interest is motivated by problems in star formation. Over the past few years, the authors have been members of two parallel code development efforts, and this review reflects that organization. In particular, we discuss numerical methods for MHD as implemented in the Athena code, and numerical methods for radiation hydrodynamics as implemented in the Orion code. We discuss the challenges introduced by the use of adaptive mesh refinement in both codes, as well as the most promising directions for future developments.

---

## 1. Introduction

The dynamics of astrophysical systems described by the equations of radiation magnetohydrodynamics (MHD) span a tremendous range of scales and parameter regimes, from the interiors of stars, e.g. Kippenhahn & Weigert (1994), to accretion disks around compact objects, e.g. Turner *et al.* (2003), to dusty accretion flows around massive protostars, e.g. Krumholz *et al.* (2005), Krumholz *et al.* (2007a), to galactic-scale flows onto AGN, e.g. Thompson *et al.* (2005). All of these systems have in common that matter, radiation and magnetic fields are strongly interacting, and that the energy and momentum carried by the radiation field is significant in comparison to that carried by the gas. Thus, an accurate treatment of the problem must include analysis of both the matter and the radiation as well as the magnetic fields, and their mutual interaction.

Numerical methods are essential to generate time-dependent and multidimensional solutions to the nonlinear equations of radiation MHD. In fact, numerical methods for both MHD and radiation hydrodynamics are in and of themselves active areas of development, let alone for the combined system of radiation MHD. Our goal in this review is to discuss the current status of numerical methods for radiation MHD, with emphasis on the challenges and areas where further development is needed. However, in order to clarify the discussion we will describe methods for MHD and those for radiation hydrodynamics in separate sections, using examples drawn from two separate efforts. In particular, we will use the MHD algorithms implemented in the Athena code (developed by Stone and collaborators) to demonstrate the issues and challenges associated with higher-order Godunov methods for MHD using adaptive mesh refinement (AMR), while we will use the radiation hydrodynamics algorithms implemented in the Orion code (developed by Klein and collaborators) to demonstrate the challenges associated with higher-order Godunov methods for radiation hydrodynamics using AMR. Our focus is on a discussion of the fundamental issues for numerical algorithms in each of these areas, rather than a step-by-step description of the actual codes (for a thorough discussion of the algorithms in Athena, see Gardiner & Stone (2005), Gardiner & Stone (2007), and Stone *et al.* (2007), while for the Orion code see Truelove *et al.* (1998), Klein (1999), Fisher (2002), Crockett *et al.* (2005) and Krumholz *et al.* (2007b).

In addition to a discussion of methods for MHD (in §2) and radiation hydrodynamics (in §3), we shall also discuss the issues associated with the implementation of AMR (in §4), as well as directions for future research (in §5).

## 2. Magnetohydrodynamic Algorithms: The Athena Code

### 2.1. *Introduction*

There are a wide range of algorithms that have been developed to solve the equations of compressible MHD. For example, the ZEUS code (Stone & Norman 1992) implements methods based on operator splitting a non-conservative formulation of the equations of motion. However, operator split methods based on the non-conservative formulation are not suitable for use with AMR, and therefore in recent years there has been a surge in development of higher-order Godunov methods for MHD.

In this section, we describe directionally-unsplit, higher-order Godunov methods for MHD as implemented in the Athena code (Gardiner & Stone 2005; 2007, hereafter GS05 and GS07 respectively). Other codes that implement similar methods include Riemann (Balsara 2001), Nirvana (Ziegler 2005), RAMSES (Fromang, Hennebelle, & Teyssier 2006), PLUTO (Mignone et al. 2007), and AstroBEAR (Cunningham et al. 2007). The primary differences between the algorithms implemented in these codes are two-fold: (1) the multidimensional integration algorithm, and (2) the method by which the divergence-free constraint on the magnetic field is enforced. Some of the different options that have been explored include unconstrained directionally split integrators (Dai & Woodward 1994), or directionally split and unsplit integrators that use either a Hodge projection to enforce the constraint (Zachary, Malagoli, & Colella 1994; Ryu, Jones, & Frank 1995; Balsara 1998; Crockett et al. 2005), a non-conservative formulation that allows propagation and damping of errors in the constraint (Powell 1994; Falle, Komissarov, & Joarder 1998; Powell et al. 1999; Dedner et al. 2002), or some form of the constrained transport (CT) algorithm of Evans & Hawley (1988) to enforce the constraint (Dai & Woodward 1998; Ryu et al. 1998; Balsara & Spicer 1999; Tóth 2000; Pen, Arras, & Wong 2003; Londrillo & Del Zanna 2004; Ziegler 2005; Fromang, Hennebelle, & Teyssier 2006; Mignone et al. 2007). A systematic comparison between many of these methods is provided by Tóth (2000).

Over the past several years during the development of Athena, we have explored many of the same ideas described in the above papers as the basis of explicit numerical algorithm for ideal MHD. We have focused our effort on three aspects. The first is the use of the CT algorithm to preserve the divergence free constraint, the second is the use of a directionally unsplit integrator to update the equations of motion, and the third is the use of the piecewise parabolic method (PPM) of Colella & Woodward (1984) for the reconstruction of interface states in multidimensional MHD. Along the way, we have found a number of modifications and extensions that are required to make a robust and accurate MHD algorithm based on these three ingredients. In particular we have found that (1) the method by which the Godunov fluxes are used to calculate the electric fields needed by CT requires a more sophisticated approach than simple arithmetic averaging, (2) using the corner transport upwind (CTU) method of Colella (1990) as a directionally unsplit integration algorithm requires the addition of “source terms” for MHD during the interface state correction steps, and (3) the extension of the dimensionally-split spatial reconstruction scheme in PPM requires similar source terms for multidimensional MHD. It is beyond the scope of this review to describe each of these extensions in detail. However, after introducing the equations of motion for MHD, and describing their

discretization in the following subsections, we will provide an overview of each of three ingredients in order to motivate the extensions implemented in Athena. Most of this section will focus on the results of a set of test problems that we have found extremely insightful for benchmarking MHD algorithms.

### 2.2. The Equations of MHD

Athena solves the equations of ideal MHD in conservative form

$$\frac{\partial \rho}{\partial t} + \nabla \cdot (\rho \mathbf{v}) = 0 \quad (2.1)$$

$$\frac{\partial \rho \mathbf{v}}{\partial t} + \nabla \cdot (\rho \mathbf{v} \mathbf{v} - \mathbf{B} \mathbf{B}) + \nabla P^* = 0 \quad (2.2)$$

$$\frac{\partial E}{\partial t} + \nabla \cdot ((E + P^*) \mathbf{v} - \mathbf{B}(\mathbf{B} \cdot \mathbf{v})) = 0 \quad (2.3)$$

$$\frac{\partial \mathbf{B}}{\partial t} + \nabla \times (\mathbf{v} \times \mathbf{B}) = 0 \quad (2.4)$$

where  $P^*$  is the total pressure (gas plus magnetic),  $E$  is the total energy density, and we have chosen a system of units in which the magnetic permeability  $\mu = 1$ . The other symbols have their usual meaning. We use an ideal gas equation of state for which  $P = (\gamma - 1)\epsilon$ , where  $\gamma$  is the ratio of specific heats, so that the internal energy density  $\epsilon$  is related to the total energy  $E$  via

$$E \equiv \epsilon + \rho(\mathbf{v} \cdot \mathbf{v})/2 + (\mathbf{B} \cdot \mathbf{B})/2. \quad (2.5)$$

Note that no explicit resistivity or viscosity is included in the above equations. We will restrict our discussion in this paper to algorithms for ideal MHD.

### 2.3. Discretization

The above equations are discretized using a control-volume approach, with volume averages of the density, total energy, and momentum stored at cell-centers, and area averages of the magnetic field stored at cell-faces. This results in a staggered grid for the magnetic field. We have argued (GS05) that although a staggered grid introduces additional complexity into the coding of the algorithm, it is the most natural representation of the discrete form of the induction equation. That is because the integral form of the induction equation uses Stoke's Law to relate the time-rate of change of area-averaged fields with line-averaged electric fields to conserve magnetic flux. This is in contrast to the first three of the equations of motion, in which Gauss' Law is used to relate the time-rate of change of volume-averaged quantities to their area-averaged fluxes.

Integration of the first three equation over a grid cell, and over a discrete interval of time  $\delta t$  gives, after application of the divergence theorem,

$$\begin{aligned} \mathbf{U}_{i,j,k}^{n+1} = \mathbf{U}_{i,j,k}^n & - \frac{\delta t}{\delta x} \left( \mathbf{F}_{i+1/2,j,k}^{n+1/2} - \mathbf{F}_{i-1/2,j,k}^{n+1/2} \right) \\ & - \frac{\delta t}{\delta y} \left( \mathbf{G}_{i,j+1/2,k}^{n+1/2} - \mathbf{G}_{i,j-1/2,k}^{n+1/2} \right) \\ & - \frac{\delta t}{\delta z} \left( \mathbf{H}_{i,j,k+1/2}^{n+1/2} - \mathbf{H}_{i,j,k-1/2}^{n+1/2} \right) \end{aligned} \quad (2.6)$$

where  $\mathbf{U}_{i,j,k}^n$  is a vector of volume-averaged variables, while  $\mathbf{F}_{i-1/2,j,k}^{n+1/2}$ ,  $\mathbf{G}_{i,j-1/2,k}^{n+1/2}$ , and  $\mathbf{H}_{i,j,k-1/2}^{n+1/2}$  are their area-averaged fluxes at the  $x$ ,  $y$ , and  $z$ -interfaces. We have used the notation that integer subscripts denote cell-centers, and half-integer subscripts denote cell

faces. The calculation of the time-averaged fluxes is described in §2.5. The components of  $\mathbf{U}_{i,j,k}^n$  are the mass density, each component of the momentum, and the total energy.

In contrast to the finite-volume difference formulae given above, the discrete form of the induction equation comes from integration of equation 2.4 over the three orthogonal faces of the cell located at  $(i - 1/2, j, k)$ ,  $(i, j - 1/2, k)$  and  $(i, j, k - 1/2)$  respectively, gives

$$\begin{aligned} B_{x,i-1/2,j,k}^{n+1} &= B_{x,i-1/2,j,k}^n - \frac{\delta t}{\delta y} (\mathcal{E}_{z,i-1/2,j+1/2,k}^{n+1/2} - \mathcal{E}_{z,i-1/2,j-1/2,k}^{n+1/2}) \\ &\quad + \frac{\delta t}{\delta z} (\mathcal{E}_{y,i-1/2,j,k+1/2}^{n+1/2} - \mathcal{E}_{y,i-1/2,j,k-1/2}^{n+1/2}) \end{aligned} \quad (2.7)$$

$$\begin{aligned} B_{y,i,j-1/2,k}^{n+1} &= B_{y,i,j-1/2,k}^n + \frac{\delta t}{\delta x} (\mathcal{E}_{z,i+1/2,j-1/2,k}^{n+1/2} - \mathcal{E}_{z,i-1/2,j-1/2,k}^{n+1/2}) \\ &\quad - \frac{\delta t}{\delta z} (\mathcal{E}_{x,i,j-1/2,k+1/2}^{n+1/2} - \mathcal{E}_{x,i,j-1/2,k-1/2}^{n+1/2}) \end{aligned} \quad (2.8)$$

$$\begin{aligned} B_{z,i,j,k-1/2}^{n+1} &= B_{z,i,j,k-1/2}^n - \frac{\delta t}{\delta x} (\mathcal{E}_{y,i+1/2,j,k-1/2}^{n+1/2} - \mathcal{E}_{y,i-1/2,j,k-1/2}^{n+1/2}) \\ &\quad + \frac{\delta t}{\delta y} (\mathcal{E}_{x,i,j+1/2,k-1/2}^{n+1/2} - \mathcal{E}_{x,i,j-1/2,k-1/2}^{n+1/2}) \end{aligned} \quad (2.9)$$

where  $B_{x,i-1/2,j,k}^{n+1}$ , etc., are the time- and area-averaged components of the magnetic field located at the cell faces. The time and line-averaged electric field  $\mathcal{E}_{z,i-1/2,j+1/2,k}^{n+1/2}$ , etc. is located at cell edges, and must be computed from the fluxes returned by the Riemann solver described in §2.5. It is easy to show the above discretization of the induction equation preserves the divergence free constraint on the magnetic field exactly, on a cell-by-cell basis. This is the advantage of using the staggered grid formulation of CT.

In Athena, the primary description of the magnetic field is taken to be the face-centered area-averages. However, cell-centered values for the field are needed to construct the fluxes of momentum and energy. Here, we adopt the second-order accurate averages

$$B_{x,i,j,k} = \frac{1}{2}(B_{x,i+1/2,j,k} + B_{x,i-1/2,j,k}), \quad (2.10)$$

$$B_{y,i,j,k} = \frac{1}{2}(B_{y,i,j+1/2,k} + B_{y,i,j-1/2,k}), \quad (2.11)$$

$$B_{z,i,j,k} = \frac{1}{2}(B_{z,i,j,k+1/2} + B_{z,i,j,k-1/2}). \quad (2.12)$$

## 2.4. Spatial Reconstruction

In a Godunov method, time-averaged fluxes of the conserved quantities at each interface are computed using a Riemann solver. This requires a spatial reconstruction step to interpolate the conserved quantities to cell faces. In Athena, we adopt the PPM reconstruction algorithm. We first transform from the primitive to conserved variables, and we perform the reconstruction using the primitive variables. Slope limiters are applied to keep the reconstruction monotonic, and these are based on the characteristic variables. The PPM algorithm also includes a time advance based on a characteristic decomposition of the primitive variables. All of these steps are too complex to describe in detail here; instead we refer the reader to Stone *et al.* (2007) and the references therein.

In GS05 and GS07, we have shown that for MHD the PPM interface reconstruction

algorithm requires an important extension. The time advance of the primitive variables includes terms proportional to the transverse gradients of the magnetic field. That is, in the calculation of the interface states of  $B_x$  it is necessary to include terms proportional to  $\partial B_y/\partial y$  and  $\partial B_z/\partial z$ , and similarly for the calculation of the interface states of  $B_y$  and  $B_z$ . These terms arise because the divergence-free constraint relates  $\partial B_x/\partial x$  with these transverse gradients. Of course in one-dimension  $\partial B_x/\partial x = 0$ , and these terms are not needed. However, for multidimensional MHD, they are crucial for reconstructing complex field geometries.

### 2.5. Riemann Solvers

To compute the fluxes of conserved quantities from the left- and right-states constructed above, a variety of Riemann solvers can be used. We have implemented Roe's linearized solver (Cargo & Gallice 1997), and various forms of the HLL solver (Toro 1999), as well as exact solvers for hydrodynamics. Roe's solver is accurate for all wave families, but often fails for strong rarefactions. Versions of the HLL solvers that do not include the contact wave are too diffusive for practical applications. We find the extension of HLL that includes the contact wave (called HLLC in Toro 1999) for hydrodynamics, and HLLD in Miyoshi & Kusano 2005 for MHD) is the most efficient, robust, and accurate.

### 2.6. Constrained Transport

The CT update of the magnetic field requires the line-averaged emfs at cell corners, which must be computed from the area-averaged electric fields returned by the Riemann solver. In GS05, it was shown that the relationship between the two is determined by the averaging formulae used to convert between the face-centered area-averages of the magnetic field, and the cell-centered volume-averages. A variety of different relationships (all consistent to second order) can be used, however we have found the most useful to be (suppressing the index  $k$  on all the formulae below)

$$\begin{aligned} \mathcal{E}_{z,i-1/2,j-1/2} = & \frac{1}{4} (\mathcal{E}_{z,i-1/2,j} + \mathcal{E}_{z,i-1/2,j+1} + \mathcal{E}_{z,i,j-1/2} + \mathcal{E}_{z,i+1,j-1/2}) \\ & + \frac{\delta y}{8} \left( \left( \frac{\partial \mathcal{E}_z}{\partial y} \right)_{i-1/2,j-1/4} - \left( \frac{\partial \mathcal{E}_z}{\partial y} \right)_{i-1/2,j-3/4} \right) \\ & + \frac{\delta x}{8} \left( \left( \frac{\partial \mathcal{E}_z}{\partial x} \right)_{i-1/4,j-1/2} - \left( \frac{\partial \mathcal{E}_z}{\partial x} \right)_{i-3/4,j-1/2} \right). \end{aligned} \quad (2.13)$$

where the derivative of  $\mathcal{E}_z$  on each grid cell face is computed by selecting the “upwind” direction according to the contact mode, e.g.

$$\left( \frac{\partial \mathcal{E}_z}{\partial y} \right)_{i-1/2,j-1/4} = \begin{cases} (\partial \mathcal{E}_z / \partial y)_{i-1,j-1/4} & \text{for } v_{x,i-1/2} > 0 \\ (\partial \mathcal{E}_z / \partial y)_{i,j-1/4} & \text{for } v_{x,i-1/2} < 0 \\ \frac{1}{2} \left( \left( \frac{\partial \mathcal{E}_z}{\partial y} \right)_{i-1,j-1/4} + \left( \frac{\partial \mathcal{E}_z}{\partial y} \right)_{i,j-1/4} \right) & \text{otherwise} \end{cases} \quad (2.14)$$

with an analogous expression for the  $(\partial \mathcal{E}_z / \partial x)$ . The derivatives of the electric field are computed using the face centered electric fields (Godunov fluxes) and a cell center “reference” value  $\mathcal{E}_{z,i,j}^r$ , e.g.

$$\left( \frac{\partial \mathcal{E}_z}{\partial y} \right)_{i,j-1/4} = 2 \left( \frac{\mathcal{E}_{z,i,j}^r - \mathcal{E}_{z,i,j-1/2}}{\delta y} \right). \quad (2.15)$$

Note for the 3D CTU+CT algorithm, analogous expressions to the above are required to convert the  $x$ - and  $y$ -components of the electric field to the appropriate cell corners.

GS05 discusses the derivation of the above formulae in detail, and discusses a test problem based on passive advection of a field loop that demonstrates the importance of the method, and potential failings of simple arithmetic averaging (this test is also introduced below).

### 2.7. *Directionally unsplit integrators*

In GS05 we showed that directionally-split integration methods, which are extremely powerful for hydrodynamics, cannot be used in MHD without violating the divergence-free constraint. The reason for this is simple: it is impossible to enforce the divergence-free constraint between partial updates unless all three components of the magnetic field are updated together. For this reason, we adopt the unsplit corner transport upwind (CTU) method of Colella (1990) to integrate the cell-centered quantities.

Even so, substantial modifications to CTU are required to make it work with MHD using CT. In particular, the transverse flux gradients used to correct the left- and right-states with in multidimensions must be modified with “MHD source terms”, that is terms proportional to  $\partial B_x/\partial x$ ,  $\partial B_y/\partial y$  and  $\partial B_z/\partial z$ . The derivation of the exact form of the necessary terms are given in GS05 and GS07.

### 2.8. *Tests*

One of the most important aspects of developing new numerical methods is the adoption of a test suite that can reveal differences and shortcomings of methods. We have found it is important to focus on multidimensional tests, since for MHD the numerical algorithms in multidimensions is much more complex than in one-dimension. Even plane-parallel 1D solutions are therefore computed in multidimensions, inclined at an oblique angle in order to break any symmetries. In what follows, we present results from a series of five test problems we have found particularly useful for testing MHD codes.

*Linear Wave Convergence.* We initialize linear amplitude modes from each MHD wave family on a fully 3D grid, with a wavevector inclined at angles of  $\alpha$  and  $\beta$  in the  $x-y$  and  $x-z$  planes respectively, where  $\sin \alpha = 2/3$  and  $\sin \beta = 2/\sqrt{5}$ . Figure 1 plots the L1 error norm for linear amplitude fast, slow, Alfvén, and entropy waves in a three-dimensional domain using a resolution of  $2N \times N \times N$  grid points, where  $N = 8, 16, 32, 64$ , and 128. The HLLD Riemann solver is used. This demonstrates Athena converges at second-order for all wave families in 3D. The waves propagate in a uniform medium for one crossing time of the domain. The details of the test are given in GS07 and Stone et al. (2007).

*Propagation of Circularly Polarized Alfvén Wave.* This test was introduced by Tóth (2000). A nonlinear amplitude circularly polarized Alfvén wave (which is an exact nonlinear solution to the equations of MHD) is initialized on a fully 3D grid, with a wavevector inclined at angles of  $\alpha$  and  $\beta$  in the  $x-y$  and  $x-z$  planes respectively, where  $\sin \alpha = 2/3$  and  $\sin \beta = 2/\sqrt{5}$  (as in the linear wave test above). Figure 2 plots the profile of the wave after propagating a distance of five wavelengths for a variety of different numerical resolutions, as well as the L1 error norm. The results show that with 32 or more grid points per wavelength, the wave profile is maintained extremely well. More importantly, the error in the solution converges at second-order.

*Advection of a Field Loop.* This is a challenging test for Godunov schemes using CT, since the field will be distorted or the method will be unstable if the edge-centered line-averaged electric fields are not computed from the face-centered area-averaged Godunov fluxes. Figure 3 plots the current density from a fully 3D calculation of a field cylinder inclined at an oblique angle to the grid, after being advected around the grid twice, using a grid with a resolution of  $128^3$ . The strength of the magnetic field in the loop is set to be very small, so the test is essentially the advection of a passive field. The current



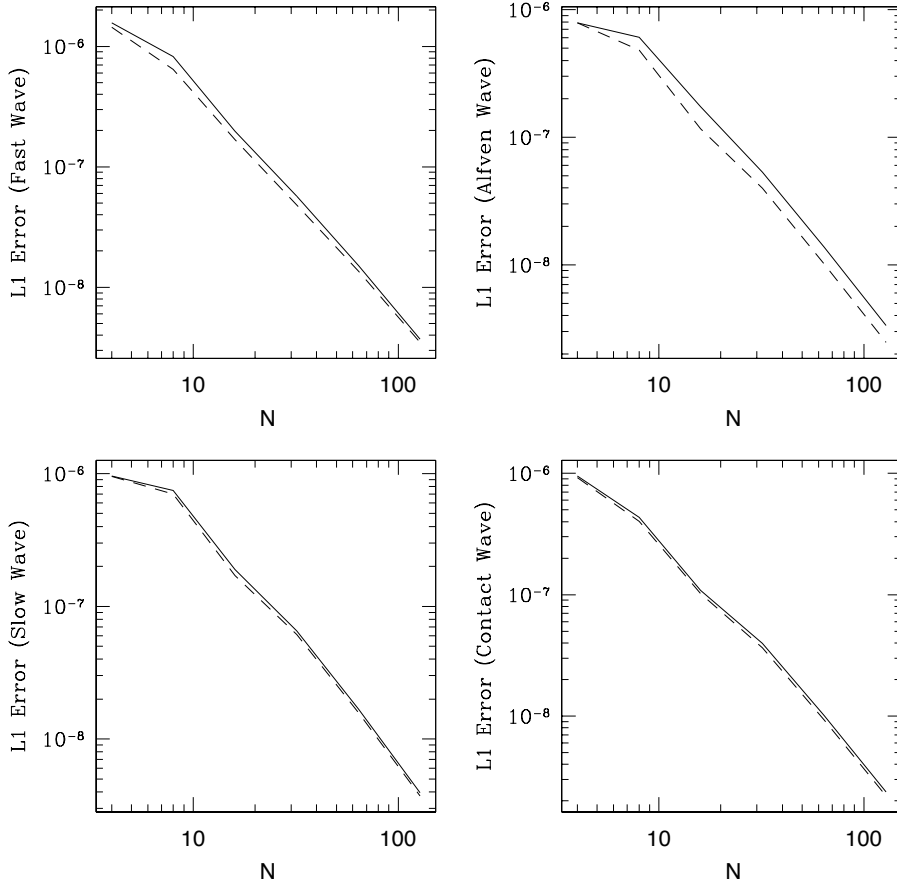


FIGURE 1. L1 error norm for each wave family in MHD as a function of grid resolution  $N$ . The solid line uses second-order (piecewise linear) reconstruction and the MUSCL-Hancock directionally unsplit integrator. The dashed line uses second-order (piecewise linear) reconstruction and the CTU directionally unsplit integrator.

distribution should be cylindrical, with a hollow core. The distribution in the figure clearly reproduces this result: thus the numerical algorithm has not seriously distorted or diffused the original shape. Details of the test are given in GS07.

*Shocktube Rotated to the Grid.* One dimensional shocktubes are a standard test of both hydrodynamics and MHD codes. However, to make the test challenging, we use a fully 3D grid, and rotate the initial discontinuity to the mesh at an oblique angle. Some care is required to ensure the divergence free constraint is maintained in the initial conditions; a complete description of the initialization of this test is given in GS07. Figure 4 shows profiles across the mesh of various quantities for the Riemann problem given in Ryu & Jones (1995) in their figure 2a (thus, we refer to this test as the RJ2a test). The grid resolution is  $768 \times 8 \times 8$ . The test is of particular interest, since the initial conditions result in discontinuities in every wave family that propagate away from the initial interface (that is both fast and slow magnetosonic shocks, and rotational and contact discontinuities). The profiles shown in figure 4 can be compared to the 1D

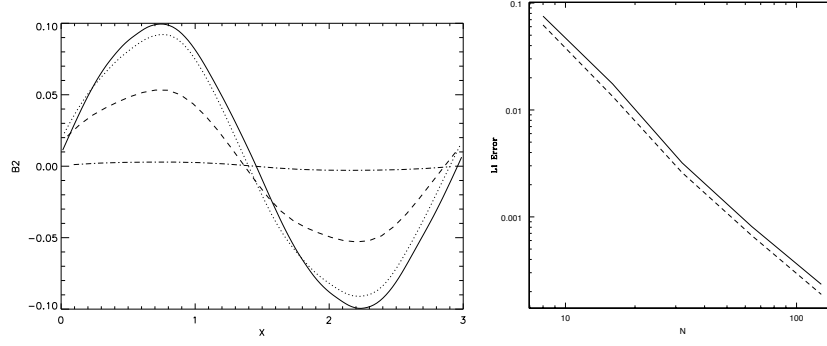


FIGURE 2. (*Left.*) Profile of nonlinear amplitude circularly polarized Alfvén wave after propagating five wavelengths on a fully 3D grid with resolution  $2N \times N \times N$ , where  $N = 64$  (solid line), 32 (dashed line), 16 (dashed line), and 8 (dash-dotted line). (*Right.*) L1 errors in solution as a function of resolution  $N$ .

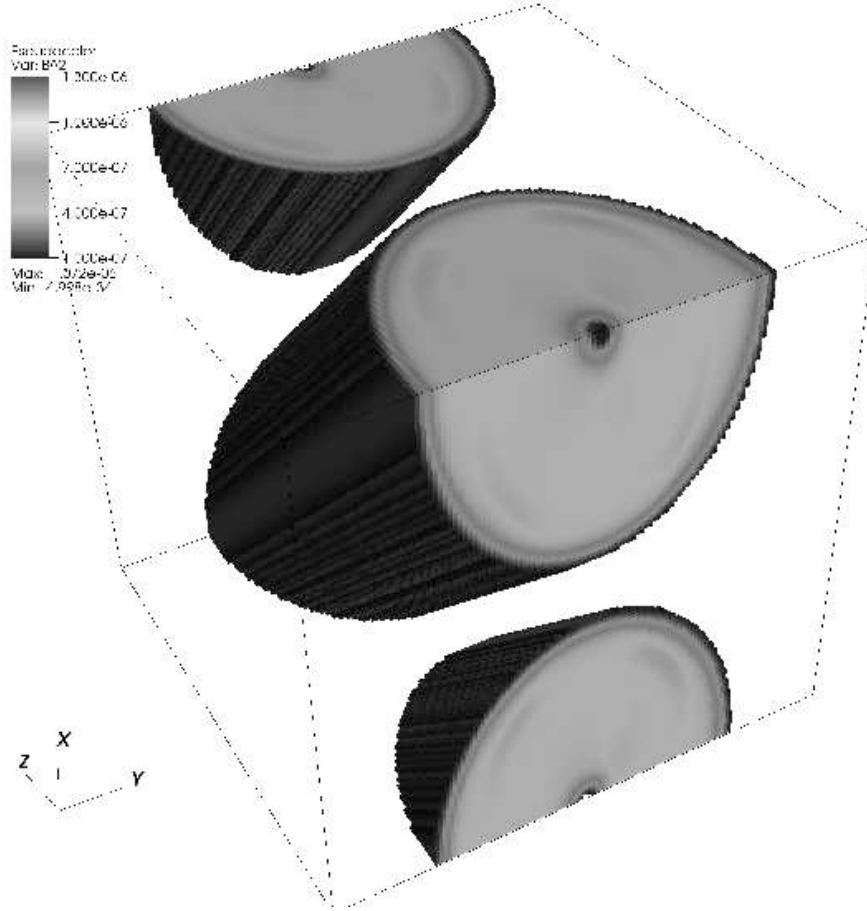


FIGURE 3. Distribution of the amplitude of the current density  $|\mathbf{J}| = |\nabla \times \mathbf{B}|$  in a cylindrical field loop inclined at an oblique angle to the grid, after being advected across the grid diagonal twice. The distribution shows little evolution from the initial conditions.

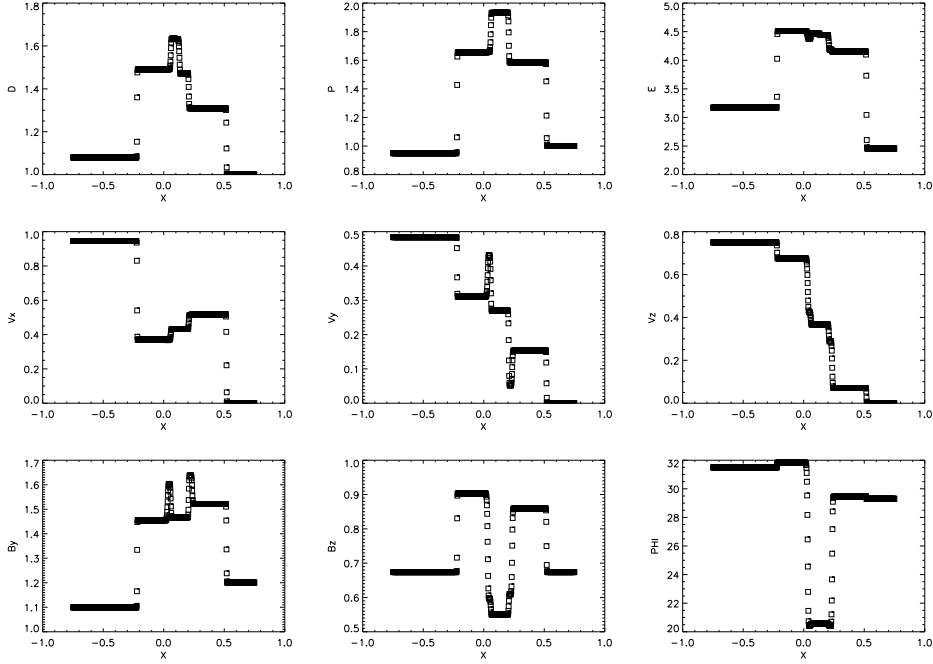


FIGURE 4. From left to right, and top to bottom, profiles of the density, pressure, total energy, three components of velocity, the two transverse components of the magnetic field  $B_y$  and  $B_z$ , and the rotation angle  $\arctan B_z/B_y$  for the RJ2a Riemann problem run in full 3D at an oblique angle to the grid.

solution shown in Ryu & Jones (1995) and elsewhere. Note all seven waves are reproduced well, with a fidelity comparable to the 1D solution. No extraneous ringing is seen in the velocity or magnetic field components in comparison to 1D, which would be an indication of problems maintaining the divergence free constraint.

*MHD Blast Wave.* The final test has no analytic solution, but is a good check on how robust is the algorithm on fully dynamic problems, and whether it can hold spherical symmetry. A spherical region with pressure 100 times larger than ambient is initialized at the center of the grid, with a strong magnetic field inclined at  $45^\circ$  to the mesh. This results in the production of a strong, spherical blast wave which propagates outward, as well as a rarefaction which propagates inward. The geometrical focusing of the rarefaction towards the center of the region can cause numerical problems. Figure 5 plots contours of the density and magnetic pressure at late time during the evolution of the blast wave. Note the contours are very smooth (no oscillations), and show the appropriate symmetries. This indicates the unsplit integrator maintains symmetries extremely well. More results and further discussion is given in GS07 and Stone et al. (2007).

### 3. Radiation–Hydrodynamic Algorithms: The Orion Code

Numerical methods exist to simulate radiation–hydrodynamical systems in a variety of dimensionalities and levels of approximation. In three dimensions, treatments of the matter and radiation fields generally adopt the flux-limited diffusion approximation, first introduced by Alme & Wilson(1973), for reasons of computational cost and simplicity e.g. Hayes *et al.* (2006). Flux-limited diffusion is optimal for treating continuum transfer

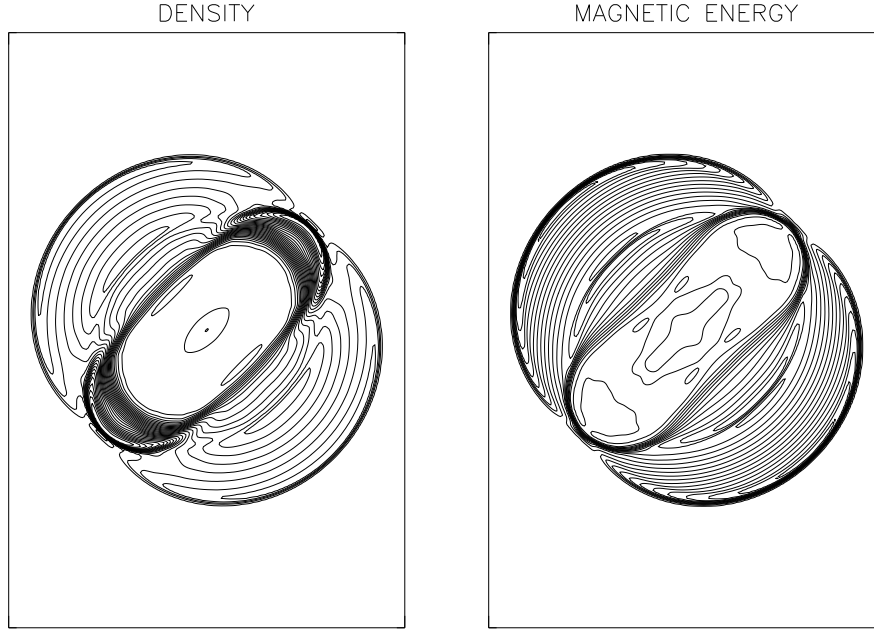


FIGURE 5. Contours of the density and magnetic energy in a slice through the center of a strong, spherical blast wave in a magnetized ambient medium. Thirty contours between the min and max are shown. Initially the magnetic field is inclined at  $45^\circ$  to the grid.

in a system such as an accretion disk, stellar atmosphere, or opaque interstellar gas cloud where the majority of the interesting behavior occurs in optically thick regions that are well described by pure radiation diffusion, but there is a surface of optical depth unity from which energy is radiated away. Applying pure diffusion to these problems would lead to unphysically fast radiation from this surface, so flux-limited diffusion provides a compromise that yields a computationally simple and accurate description of the interior, while also giving a reasonably accurate loss rate from the surface (Castor(2004)).

However, the level of accuracy provided by this approximation has been unclear because the equations of radiation hydrodynamics for flux-limited diffusion have previously only been analyzed to zeroth order in  $v/c$ . In contrast, several authors have analyzed the radiation hydrodynamic equations in the general case to beyond first order in  $v/c$  (e.g. Mihalas & Weibel-Mihalas(1999), Castor(2004)). In a zeroth order treatment, one neglects differences between quantities in the laboratory frame and the comoving frame. The problem with this approach is that in an optically thick fluid, the radiation flux only follows Fick's law ( $\mathbf{F} \propto -\nabla E$ ) in the comoving frame, and in other frames there is an added advective flux of radiation enthalpy, as first demonstrated by Castor(1972). In certain regimes (i.e. the dynamic diffusion limit – see below) this advective flux can dominate the diffusive flux (Mihalas & Auer(2001), Castor(2004)).

Mihalas & Klein(1982) were the first to derive the mixed frame equations of radiation hydrodynamics dynamics to order  $v/c$  in frequency-integrated and frequency-dependent forms, and gave numerical algorithms for solving them. Lowrie *et al.*(1999), Lowrie & Morel(2001), and Hubeny & Burrows(2006) give alternate forms of these equations, as well as numerical algorithms for solving them. However, these treatments require that one solve the radiation momentum equation (and for the frequency-dependent equations

calculate over many frequencies as well), rather than adopt the flux-limited diffusion approximation. While this is preferable from a standpoint of accuracy, since it allows explicit conservation of both momentum and energy and captures the angular-dependence of the radiation field in a way that diffusion methods cannot, treating the radiation momentum equation is significantly more computationally costly than using flux-limited diffusion, making it difficult to use in three-dimensional calculations.

In this section we analyze the equations of radiation hydrodynamics and the algorithms implemented in the Orion code following our work described in Krumholz *et al.* (2007b) under the approximations that the radiation field obeys the flux-limited diffusion approximation, and that scattering is negligible for the system. We derive an accurate set of mixed frame equations meaning that radiation quantities are written in the lab frame, but fluid quantities, in particular fluid opacities, are evaluated in the frame comoving with the fluid. This formulation is optimal for three-dimensional simulations applicable to star formation regimes, because writing radiation quantities in the lab frame lets us use an Eulerian grid on which the radiative transfer problem may be solved by any number of standard methods, while avoiding the need to model the direction- and velocity-dependence of the lab frame opacity and emissivity of a moving fluid.

We begin from the general lab frame equations of radiation hydrodynamics to first order in  $v/c$ , apply the flux-limited diffusion approximation in the frame comoving with the gas where it is applicable, and transform the appropriate radiation quantities into the lab frame, thereby deriving the corresponding mixed frame equations suitable for implementation in numerical simulations. We retain enough terms to ensure that we achieve order unity accuracy in all regimes, and order  $v/c$  accuracy for static diffusion problems. We assess the significance of the higher order terms that appear in our equations, and consider where treatments omitting them are acceptable, and where they are likely to fail. We show that, in at least some regimes, the zeroth order treatments most often used are likely to produce results that are incorrect at order unity. We also compare our equations to the comoving frame equations commonly used in other codes. We take advantage of the ordering of terms we derive for the static diffusion regime to construct a radiation hydrodynamic simulation algorithm for static diffusion problems that is simpler and faster than those now in use, which we implement in the Orion adaptive mesh refinement code. In § 3.6 we discuss a selection of radiation-hydrodynamic test problems. In the discussion that follows, we adopt the convention of writing quantities measured in the frame comoving with a fluid with a subscript zero. Quantities in the lab frame are written without subscripts. Also note that we follow the standard convention in radiation hydrodynamics rather than the standard in astrophysics, in that when we refer to an opacity  $\kappa$  we mean the total opacity, measured in units of inverse length, rather than the specific opacity, measured in units of length squared divided by mass. Since we are neglecting scattering, we may set the extinction  $\chi = \kappa$ .

### 3.1. Limiting Regimes of Radiation Hydrodynamics

It is useful to first examine some characteristic dimensionless numbers for a radiation hydrodynamic system, since evaluating these quantities provides a useful guide to how we should analyze our equations. Let  $\ell$  be the characteristic size of the system under consideration,  $u$  be the characteristic velocity in this system, and  $\lambda_P \sim 1/\kappa$ , be the photon mean free path. Following Mihalas & Weibel-Mihalas (1999), we can define three distinct limiting cases by considering the dimensionless ratios  $\tau \equiv \ell/\lambda_P$ , which characterizes the optical depth of the system, and  $\beta \equiv u/c$ , which characterizes how relativistic it is. Since we focus on non-relativistic systems, we assume  $\beta \ll 1$ . We term the case  $\tau \ll 1$ , in which the radiation and gas are weakly coupled, the *streaming* limit. If  $\tau \gg 1$  then radiation

and gas are strongly coupled, and the system is in the diffusion limit. We can further subdivide the diffusion limit into the cases  $\beta \gg \tau^{-1}$  and  $\beta \ll \tau^{-1}$ . The former is the *dynamic diffusion* limit, while the latter is the *static diffusion* limit. In summary, the limiting cases are

$$\tau \ll 1, \quad (\text{streaming limit}) \quad (3.1)$$

$$\tau \gg 1, \beta\tau \ll 1, \quad (\text{static diffusion limit}) \quad (3.2)$$

$$\tau \gg 1, \beta\tau \gg 1, \quad (\text{dynamic diffusion limit}). \quad (3.3)$$

Physically, the distinction between static and dynamic diffusion is that in dynamic diffusion radiation is principally transported by advection by gas, so that terms describing the work done by radiation on gas and the advection of radiation enthalpy dominate over terms describing either diffusion or emission and absorption. In the static diffusion limit the opposite holds. A paradigmatic example of a dynamic diffusion system is a stellar interior. The optical depth from the core to the surface of the Sun is  $\tau \sim 10^{11}$ , and typical convective and rotational velocities are  $\gg 10^{-11}c = 0.3 \text{ cm s}^{-1}$ , so the Sun is strongly in the dynamic diffusion regime. In contrast, an example of a system in the static diffusion limit is a relatively cool, dusty, outer accretion disk around a forming massive protostar, as studied e.g. by Krumholz *et al.* (2007a). The specific opacity of gas with the standard interstellar dust abundance to infrared photons is  $\kappa/\rho \sim 1 \text{ cm}^2 \text{ g}^{-1}$ , and at distances of more than a few AU from the central star the density is generally  $\rho \lesssim 10^{-12} \text{ g cm}^{-3}$ . For a disk of scale height  $h \sim 10 \text{ AU}$ , the optical depth to escape is

$$\tau^{-1} \approx 6.7 \times 10^{-3} \left( \frac{\kappa/\rho}{\text{cm}^2 \text{ g}^{-1}} \right)^{-1} \left( \frac{\rho}{10^{-12} \text{ g cm}^{-3}} \right)^{-1} \left( \frac{h}{10 \text{ AU}} \right)^{-1}. \quad (3.4)$$

The velocity is roughly the Keplerian speed, so

$$\beta \approx 1.4 \times 10^{-4} \left( \frac{M_*}{10 M_\odot} \right)^{1/2} \left( \frac{r}{10 \text{ AU}} \right)^{-1/2}, \quad (3.5)$$

where  $M_*$  is the mass of the star and  $r$  is the distance from it. Thus, this system is in a static diffusion regime by roughly two orders of magnitude.

In the development of a self-consistent formulation of radiation hydrodynamics our goal will be to obtain expressions that are accurate for the leading terms in all regimes. This is somewhat tricky, particularly for diffusion problems, because we are attempting to expand our equations simultaneously in the two small parameters  $\beta$  and  $1/\tau$ . The most common approach in radiation hydrodynamics is to expand expressions in powers of  $\beta$  alone, and only analyze the equations in terms of  $\tau$  after dropping terms of high order in  $\beta$ . However, this approach can produce significant errors, because terms in the radiation hydrodynamic equations proportional to the opacity are multiplied by a quantity of order  $\tau$ . Thus, in our derivation (Krumholz *et al.* (2007b)) we will repeatedly encounter expressions proportional to  $\beta^2\tau$ , and in a problem that is either in the dynamic diffusion limit or close to it ( $\beta\tau \gtrsim 1$ ), it is inconsistent to drop these terms while retaining ones that are of order  $\beta$ . We therefore retain all terms up to order  $\beta^2$  in our derivation unless we explicitly check that they are not multiplied by terms of order  $\tau$ , and can therefore be dropped safely.

3.2. *The Equations of Radiation Hydrodynamics*

We begin with the lab frame equations of radiation hydrodynamics (e.g. Mihalas & Klein(1982), Mihalas & Weibel-Mihalas(1999), Mihalas & Auer(2001))

$$\frac{\partial \rho}{\partial t} + \nabla \cdot (\rho \mathbf{v}) = 0 \quad (3.6)$$

$$\frac{\partial}{\partial t}(\rho \mathbf{v}) + \nabla \cdot (\rho \mathbf{v} \mathbf{v}) = -\nabla P + \mathbf{G} \quad (3.7)$$

$$\frac{\partial}{\partial t}(\rho e) + \nabla \cdot [(\rho e + P) \mathbf{v}] = cG^0 \quad (3.8)$$

$$\frac{\partial E}{\partial t} + \nabla \cdot \mathbf{F} = -cG^0 \quad (3.9)$$

$$\frac{1}{c^2} \frac{\partial \mathbf{F}}{\partial t} + \nabla \cdot \mathcal{P} = -\mathbf{G} \quad (3.10)$$

where  $\rho$ ,  $\mathbf{v}$ ,  $e$ , and  $P$  are the density, velocity, specific energy (thermal plus kinetic), and thermal pressure of the gas,  $E$ ,  $\mathbf{F}$ , and  $\mathcal{P}$  are the radiation energy density, flux, and pressure tensor,

$$cE = \int_0^\infty d\nu \int d\Omega I(\mathbf{n}, \nu) \quad (3.11)$$

$$\mathbf{F} = \int_0^\infty d\nu \int d\Omega \mathbf{n} I(\mathbf{n}, \nu) \quad (3.12)$$

$$c\mathcal{P} = \int_0^\infty d\nu \int d\Omega \mathbf{n} \mathbf{n} I(\mathbf{n}, \nu), \quad (3.13)$$

$(G^0, \mathbf{G})$  is the radiation four-force density

$$cG^0 = \int_0^\infty d\nu \int d\Omega [\kappa(\mathbf{n}, \nu) I(\mathbf{n}, \nu) - \eta(\mathbf{n}, \nu)], \quad (3.14)$$

$$c\mathbf{G} = \int_0^\infty d\nu \int d\Omega [\kappa(\mathbf{n}, \nu) I(\mathbf{n}, \nu) - \eta(\mathbf{n}, \nu)] \mathbf{n}, \quad (3.15)$$

and  $I(\mathbf{n}, \nu)$  is the intensity of the radiation field at frequency  $\nu$  traveling in direction  $\mathbf{n}$ . Here  $\kappa(\mathbf{n}, \nu)$  and  $\eta(\mathbf{n}, \nu)$  are the direction- and frequency-dependent radiation absorption and emission coefficients in the lab frame. Essentially,  $cG^0$  is the rate of energy absorption from the radiation field minus the rate of energy emission for the fluid, and  $\mathbf{G}$  is the rate of momentum absorption from the radiation field minus the rate of momentum emission. Equations (3.6) – (3.8) are accurate to first order in  $v/c$ , while equations (3.9) – (3.10) are exact. Since no terms involving opacity or optical depth appear explicitly in any of these equations, so the fact that they are accurate to first order in  $\beta$  means that they include all the leading order terms.

In order to derive the mixed-frame equations, we first evaluate the radiation four-force  $(G^0, \mathbf{G})$  in terms of lab frame radiation quantities and comoving frame emission and absorption coefficients. Mihalas & Auer(2001) show that, if the flux spectrum of the radiation is direction-independent, the radiation four-force on a thermally-emitting material to all orders in  $v/c$  is given in terms of moments of the radiation field by

$$\begin{aligned} G^0 &= \gamma[\gamma^2 \kappa_{0E} + (1 - \gamma^2) \kappa_{0F}] E - \gamma \kappa_{0P} a_R T_0^4 \\ &\quad - \gamma(\mathbf{v} \cdot \mathbf{F}/c^2) [\kappa_{0F} - 2\gamma^2(\kappa_{0F} - \kappa_{0E})] \\ &\quad - \gamma^3(\kappa_{0F} - \kappa_{0E})(\mathbf{v} \mathbf{v}) : \mathcal{P}/c^2, \\ \mathbf{G} &= \gamma \kappa_{0F} (\mathbf{F}/c) - \gamma \kappa_{0P} a_R T_0^4 (\mathbf{v}/c) \end{aligned} \quad (3.16)$$

$$\begin{aligned}
& - [\gamma^3(\kappa_{0F} - \kappa_{0E})(\mathbf{v}/c)E + \gamma\kappa_{0F}(\mathbf{v}/c) \cdot \mathcal{P}] \\
& + \gamma^3(\kappa_{0F} - \kappa_{0E})[2\mathbf{v} \cdot \mathbf{F}/c^3 - (\mathbf{v}\mathbf{v}) : \mathcal{P}/c^3]\mathbf{v},
\end{aligned} \tag{3.17}$$

where  $\gamma = 1/\sqrt{1 - v^2/c^2}$  is the Lorentz factor and  $T_0$  is the gas temperature. The three opacities that appear are the Planck-, energy-, and flux-mean opacities, which are defined by

$$\kappa_{0P} = \frac{\int_0^\infty d\nu_0 \kappa_0(\nu_0) B(\nu_0, T_0)}{B(T_0)} \tag{3.18}$$

$$\kappa_{0E} = \frac{\int_0^\infty d\nu_0 \kappa_0(\nu_0) E_0(\nu_0)}{E_0} \tag{3.19}$$

$$\kappa_{0F} = \frac{\int_0^\infty d\nu_0 \kappa_0(\nu_0) \mathbf{F}_0(\nu_0)}{\mathbf{F}_0}, \tag{3.20}$$

where  $E_0(\nu_0)$  and  $\mathbf{F}_0(\nu_0)$  are the comoving frame radiation energy and flux per unit frequency,  $E_0$  and  $\mathbf{F}_0$  are the corresponding frequency-integrated energy and flux, and  $B(\nu, T) = (2h\nu^3/c^2)/(e^{h\nu/k_B T} - 1)$  and  $B(T) = ca_R T^4/(4\pi)$  are the frequency-dependent and frequency-integrated Planck functions.

Note that we have implicitly assumed that the opacity and emissivity are directionally-independent in the fluid rest frame, which is the case for any conventional material. We have also assumed that the flux spectrum is independent of direction, allowing us to replace the flux-mean opacity vector with a scalar. This may not be the case for an optically thin system, or one in which line transport is important, but since we are limiting our application to systems to which we can reasonably apply the diffusion approximation, this is not a major limitation.

To simplify  $(G^0, \mathbf{G})$ , we make several approximations (e.g. Krumholz *et al.* (2007b)) such that the only two opacities remaining in our equations are  $\kappa_{0R}$  and  $\kappa_{0P}$ , both of which are independent of the spectrum of the radiation field and the direction of radiation propagation, and which may therefore be tabulated as a function of temperature for a given material once and for all.

Following our work in Krumholz *et al.* (2007b), we expand  $(G^0, \mathbf{G})$  in powers of  $v/c$ , retaining terms to order  $v^2/c^2$ . The resulting expression for the radiation four-force is

$$\begin{aligned}
G^0 &= \kappa_{0P} \left( E - \frac{4\pi B}{c} \right) + (\kappa_{0R} - 2\kappa_{0P}) \frac{\mathbf{v} \cdot \mathbf{F}}{c^2} \\
&+ \frac{1}{2} \left( \frac{v}{c} \right)^2 \left[ 2(\kappa_{0P} - \kappa_{0R})E + \kappa_{0P} \left( E - \frac{4\pi B}{c} \right) \right] \\
&+ (\kappa_{0P} - \kappa_{0R}) \frac{\mathbf{v}\mathbf{v} : \mathcal{P}}{c^2} + O\left(\frac{v^3}{c^3}\right)
\end{aligned} \tag{3.21}$$

$$\begin{aligned}
\mathbf{G} &= \kappa_{0R} \frac{\mathbf{F}}{c} + \kappa_{0P} \left( \frac{\mathbf{v}}{c} \right) \left( E - \frac{4\pi B}{c} \right) \\
&- \kappa_{0R} \left[ \frac{\mathbf{v}}{c} E + \frac{\mathbf{v}}{c} \cdot \mathcal{P} \right] + \frac{1}{2} \left( \frac{v}{c} \right)^2 \kappa_{0R} \frac{\mathbf{F}}{c} \\
&+ 2(\kappa_{0R} - \kappa_{0P}) \frac{(\mathbf{v} \cdot \mathbf{F})\mathbf{v}}{c^3} + O\left(\frac{v^3}{c^3}\right)
\end{aligned} \tag{3.22}$$

We can examine the scalings of these terms with the help of our dimensionless parameters  $\beta$  and  $\tau$ . In the streaming limit, radiation travels freely at  $c$  and emission and absorption of radiation by matter need not balance, so  $|\mathbf{F}| \sim cE$  and  $4\pi B/c - E \sim E$ . For static diffusion, Mihalas & Weibel-Mihalas (1999) show that  $|\mathbf{F}| \sim cE/\tau$  and  $4\pi B/c - E \sim E/\tau^2$ .



For dynamic diffusion, radiation travels primarily by advection, so  $|\mathbf{F}| \sim vE$ . We can show that for dynamic diffusion  $4\pi B/c - E \sim \beta^2 E$ . Note that the scaling  $4\pi B/c - E \sim (\beta/\tau)E$  given in Mihalas & Weibel-Mihalas(1999) appears to be incorrect. Using these values, we obtain the scalings shown in Table 1 of Krumholz *et al.* (2007b) for the terms in (3.21) and (3.22).

The Table shows that, despite the fact that we have kept all terms that are formally order  $\beta^2$  or more, in fact we only have leading-order accuracy in the dynamic diffusion limit, because in this limit the order unity and order  $\beta$  terms in  $G^0$  vanish to order  $\beta^2$ . To obtain the next-order terms, we would have had to write  $G^0$  to order  $\beta^3$ . A corollary of this is that treatments of the dynamic diffusion limit that do not retain order  $\beta^2$  terms are likely to produce equations that are incorrect at order unity, since they will have dropped terms that are of the same order as the ones that have been retained.

At this point we could begin dropping terms that are insignificant at the order to which we are working, but it is cumbersome to construct a table analogous to Table 1 at every step of our derivation. It is more convenient to continue our analysis retaining all the terms in (3.21) and (3.22), and to drop terms only periodically.

We now adopt the flux-limited diffusion approximation (e.g. Alme & Wilson(1973)), under which we drop the radiation momentum equation (3.10) and set the radiation flux in the comoving frame to

$$\mathbf{F}_0 = -\frac{c\lambda}{\kappa_{0R}} \nabla E_0, \quad (3.23)$$

where  $\lambda$  is a dimensionless number called the flux-limiter. Many functional forms for  $\lambda$  are possible. For the code implementation we adopt the Levermore & Pomraning(1981) flux-limiter and we adopt the corresponding approximate value for the radiation pressure tensor in the comoving frame  $\mathcal{P}_0$  (Levermore(1984)).

To use the approximation (3.23) and  $\mathcal{P}_0$  to evaluate the radiation four-force, we must Lorentz transform them to express the radiation quantities in the lab frame. The Lorentz transforms for the energy, flux, and pressure to second order in  $v/c$  are given in Mihalas & Weibel-Mihalas(1999)

Using the same scaling arguments that are used to construct Table 1 (Krumholz *et al.*(2007b)), we note that  $\mathcal{P}$  and  $\mathcal{P}_0$  differ at order  $\beta$  in the streaming limit, at order  $\beta/\tau$  for static diffusion, and at order  $\beta^2$  for dynamic diffusion. Since this is below our accuracy goal, we need not distinguish  $\mathcal{P}$  and  $\mathcal{P}_0$ . The same is true of  $E$  and  $E_0$ . However,  $\mathbf{F}$  is different. In the comoving frame in an optically thick system, one is in the static diffusion regime, so  $\mathbf{F}_0 \sim cE_0/\tau$ . Since  $\mathbf{v}E_0$  and  $\mathbf{v} \cdot \mathcal{P}_0$  are of order  $\beta cE_0$ , and in dynamic diffusion  $\beta \gg 1/\tau$ , this means that  $\mathbf{v}E_0$  and  $\mathbf{v} \cdot \mathcal{P}_0$  are the dominant components of  $\mathbf{F}$  in dynamic diffusion, and must therefore be retained. Thus,

$$\mathbf{F} = -\frac{c\lambda}{\kappa_{0R}} \nabla E + \mathbf{v}E + \mathbf{v} \cdot \mathcal{P}, \quad (3.24)$$

which is simply the rest frame flux plus terms describing the advection of radiation enthalpy.

Substituting  $\mathcal{P}_0$  with  $\mathcal{P} = \mathcal{P}_0$  and (3.24) into the four-force density (3.21) and (3.22), and continuing to retain terms to order  $v^2/c^2$ , gives

$$\begin{aligned} G^0 = \kappa_{0P} & \left( E - \frac{4\pi B}{c} \right) + \left( \frac{\lambda}{c} \right) \left( 2 \frac{\kappa_{0P}}{\kappa_{0R}} - 1 \right) \mathbf{v} \cdot \nabla E \\ & - \frac{\kappa_{0P}}{c^2} E \left[ \frac{3 - R_2}{2} v^2 + \frac{3R_2 - 1}{2} (\mathbf{v} \cdot \mathbf{n})^2 \right] \end{aligned}$$

$$+ \frac{1}{2} \left( \frac{v}{c} \right)^2 \kappa_{0P} \left( E - \frac{4\pi B}{c} \right) \quad (3.25)$$

$$\begin{aligned} \mathbf{G} = & -\lambda \nabla E + \kappa_{0P} \frac{\mathbf{v}}{c} \left( E - \frac{4\pi B}{c} \right) \\ & - \frac{1}{2} \left( \frac{v}{c} \right)^2 \lambda \nabla E \\ & + 2\lambda \left( \frac{\kappa_{0P}}{\kappa_{0R}} - 1 \right) \frac{(\mathbf{v} \cdot \nabla E) \mathbf{v}}{c^2}. \end{aligned} \quad (3.26)$$

Where  $R_2$  is related to  $R$  in Levermore & Pomraning(1981) and  $\mathbf{n}$  is the unit vector antiparallel to  $\nabla E$ . Although these equations contain terms of order  $\beta^2$ , they are not truly accurate to order  $\beta^2$  because we did not retain all the  $\beta^2$  when applying the Lorentz transform to the flux and pressure. However, these equations include all the terms that appear at the order of accuracy to which we are working, and by retaining terms of order  $\beta^2$  we guarantee that these terms will be preserved.

Inserting  $(G^0, \mathbf{G})$  and the lab frame flux (3.24) into the gas momentum and energy equations (3.7) and (3.8), and the radiation energy equation (3.9), and again retaining terms to order  $v^2/c^2$  gives

$$\begin{aligned} \frac{\partial}{\partial t}(\rho \mathbf{v}) = & -\nabla \cdot (\rho \mathbf{v} \mathbf{v}) - \nabla P - \lambda \nabla E \\ & - \kappa_{0P} \frac{\mathbf{v}}{c^2} (4\pi B - cE) - \frac{1}{2} \left( \frac{v}{c} \right)^2 \lambda \nabla E \\ & + 2\lambda \left( \frac{\kappa_{0P}}{\kappa_{0R}} - 1 \right) \frac{(\mathbf{v} \cdot \nabla E) \mathbf{v}}{c^2}. \end{aligned} \quad (3.27)$$

$$\begin{aligned} \frac{\partial}{\partial t}(\rho e) = & -\nabla \cdot [(\rho e + P) \mathbf{v}] - \kappa_{0P} (4\pi B - cE) \\ & + \lambda \left( 2 \frac{\kappa_{0P}}{\kappa_{0R}} - 1 \right) \mathbf{v} \cdot \nabla E \\ & - \frac{\kappa_{0P}}{c} E \left[ \frac{3 - R_2}{2} v^2 + \frac{3R_2 - 1}{2} (\mathbf{v} \cdot \mathbf{n})^2 \right] \\ & - \frac{1}{2} \left( \frac{v}{c} \right)^2 \kappa_{0P} (4\pi B - cE) \end{aligned} \quad (3.28)$$

$$\begin{aligned} \frac{\partial}{\partial t} E = & \nabla \cdot \left( \frac{c\lambda}{\kappa_{0R}} \nabla E \right) + \kappa_{0P} (4\pi B - cE) \\ & - \lambda \left( 2 \frac{\kappa_{0P}}{\kappa_{0R}} - 1 \right) \mathbf{v} \cdot \nabla E \\ & + \frac{\kappa_{0P}}{c} E \left[ \frac{3 - R_2}{2} v^2 + \frac{3R_2 - 1}{2} (\mathbf{v} \cdot \mathbf{n})^2 \right] \\ & - \nabla \cdot \left[ \frac{3 - R_2}{2} \mathbf{v} E + \frac{3R_2 - 1}{2} \mathbf{v} \cdot (\mathbf{n} \mathbf{n}) E \right] \\ & + \frac{1}{2} \left( \frac{v}{c} \right)^2 \kappa_{0P} (4\pi B - cE). \end{aligned} \quad (3.29)$$

At this point we can construct another Table (see Table 2, Krumholz *et al.*(2007b)) showing the scalings of the radiation terms to see which must be retained and which are superfluous. In constructing the table, we take spatial derivatives to be of characteristic scaling  $1/\ell$ , i.e. we assume that radiation quantities vary on a size scale of the system,

rather than over a size scale of the photon mean free path. In the streaming limit,  $\lambda \sim \tau$  and  $R_2 \sim 1 + O(\tau)$ . In the diffusion limit  $\lambda \sim 1/3$  and  $R_2 \sim 1/3 + O(\tau^{-2})$ .

Using Table 2 to drop all terms that are not significant at leading order in any regime, we arrive at our final radiation hydrodynamic equations (Krumholz *et al.* (2007b)):

$$\frac{\partial}{\partial t}(\rho \mathbf{v}) = -\nabla \cdot (\rho \mathbf{v} \mathbf{v}) - \nabla P - \lambda \nabla E \quad (3.30)$$

$$\begin{aligned} \frac{\partial}{\partial t}(\rho e) = & -\nabla \cdot [(\rho e + P) \mathbf{v}] - \kappa_{0P}(4\pi B - cE) \\ & + \lambda \left( 2 \frac{\kappa_{0P}}{\kappa_{0R}} - 1 \right) \mathbf{v} \cdot \nabla E \\ & - \frac{3 - R_2}{2} \kappa_{0P} \frac{v^2}{c} E \end{aligned} \quad (3.31)$$

$$\begin{aligned} \frac{\partial}{\partial t}E = & \nabla \cdot \left( \frac{c\lambda}{\kappa_{0R}} \nabla E \right) + \kappa_{0P}(4\pi B - cE) \\ & - \lambda \left( 2 \frac{\kappa_{0P}}{\kappa_{0R}} - 1 \right) \mathbf{v} \cdot \nabla E \\ & + \frac{3 - R_2}{2} \kappa_{0P} \frac{v^2}{c} E \\ & - \nabla \cdot \left( \frac{3 - R_2}{2} \mathbf{v} E \right). \end{aligned} \quad (3.32)$$

These represent the equations of momentum conservation for the gas, energy conservation for the gas, and energy conservation for the radiation field, which, together with the equation of mass conservation (3.6), fully describe the system under the approximations we have adopted. They are accurate and consistent to leading order in the streaming and dynamic diffusion limits. They are accurate to first order in  $\beta$  in the static diffusion limit, since we have had to retain all order  $\beta$  terms in this limit because they are of leading order in dynamic diffusion problems. Also note that if in a given problem one never encounters the dynamic diffusion regime, it is possible to drop more terms.

The equations are easy to understand intuitively. The term  $-\lambda \nabla E$  in the momentum equation (3.30) simply represents the radiation force  $\kappa_{0R} \mathbf{F}/c$ , neglecting distinctions between the comoving and laboratory frames which are smaller than leading order in this equation. Similarly, the terms  $\pm \kappa_{0P}(4\pi B - cE)$  and  $\pm \lambda(2\kappa_{0P}/\kappa_{0R} - 1) \mathbf{v} \cdot \nabla E$  in the two energy equations (3.31) and (3.32) represent radiation absorbed minus radiation emitted by the gas, and the work done by the radiation field as it diffuses through the gas. The factor  $(2\kappa_{0P}/\kappa_{0R} - 1)$  arises because the term contains contributions both from the Newtonian work and from a relativistically-induced mismatch between emission and absorption. The term proportional to  $\kappa_{0P}E/c$  represents another relativistic correction to the work, this one arising from boosting of the flux between the lab and comoving frames. In the radiation energy equation (3.32), the first term on the left hand side is the divergence of the radiation flux, i.e. the rate at which radiation diffuses, and the last term on the right hand side represents advection of the radiation enthalpy  $E + \mathcal{P}$  by the gas.

It is also worth noting that equations (3.28) and (3.29) are manifestly energy-conserving, since every term in one equation either has an obvious counterpart in the other with opposite sign, or is clearly an advection. In contrast, the momentum equation (3.30) is not manifestly momentum-conserving, since there is a force term  $-\lambda \nabla E$  with no equal and opposite counterpart. This non-conservation of momentum is an inevitable side-effect of

using the flux-limited diffusion approximation, since this approximation amounts to allowing the radiation field to transfer momentum to the gas without explicitly tracking the momentum of the radiation field and the corresponding transfer from gas to radiation.

### 3.3. The Relative Importance of Higher Order Terms

Our dynamical equations result from retaining at least some terms that are formally of order  $\beta^2$ . Even though our analysis shows that these terms can be the leading ones present, due to cancellations of lower order terms, one might legitimately ask whether they are ever physically significant. In § 3.3.1 we address this question by comparing our equations to those that result from lower order treatments. In § 3.3.2, we also compare our equations with those generally used in comoving frame formulations of radiation hydrodynamics.

To make our work in this section more transparent, we specialize to the diffusion regime in gray materials. Thus, we set  $\lambda = R_2 = 1/3$  and  $\kappa_{0P} = \kappa_{0R} = \kappa_0$ . A more general analysis produces the same conclusions. We also focus on the radiation energy equation, since all the terms that appear in the gas energy equation also appear in it, and because there are no higher order terms present in the momentum equation. Under these assumptions, our radiation energy equation (3.32) becomes

$$\begin{aligned} \frac{\partial}{\partial t} E = & \nabla \cdot \left( \frac{c}{3\kappa_0} \nabla E \right) + \kappa_0(4\pi B - cE) \\ & - \frac{4}{3} \nabla \cdot (\mathbf{v} E) - \frac{1}{3} \mathbf{v} \cdot \nabla E + \frac{4}{3} \kappa_0 \frac{v^2}{c} E. \end{aligned} \quad (3.33)$$

#### 3.3.1. Comparison to Lower Order Equations

A common approach in radiation-hydrodynamic problems is to expand the equations in  $\beta$ , rather than in both  $\beta$  and  $\tau$  as we have done, and drop at least some terms that are of order  $\beta^2$  in every regime (Mihalas & Weibel-Mihalas(1999)). To determine how equations derived in this manner compare to our higher order treatment, we compare our simplified energy equation (3.33) to the corresponding equation one would obtain by following this procedure with (3.32). This resulting energy equation is

$$\begin{aligned} \frac{\partial}{\partial t} E = & \nabla \cdot \left( \frac{c}{3\kappa_0} \nabla E \right) + \kappa_0(4\pi B - cE) \\ & - \frac{4}{3} \nabla \cdot (\mathbf{v} E) - \frac{1}{3} \mathbf{v} \cdot \nabla E. \end{aligned} \quad (3.34)$$

*We show below, equation (3.34) is not accurate to leading order in at least some cases, and should not be used for computations unless one carefully checks that the missing terms never become important in the regime covered by the computation.*

Compared to the energy equation (3.33) that we obtain by retaining all leading order terms in  $\beta$  and  $\tau$ , (3.34) is missing the term  $(4/3)\kappa_0 v^2 E/c$ . We can describe the  $\mathbf{v} \cdot \nabla E$  term as the “diffusion work” arising from the combination of the diffusion flux and the post-Newtonian emission-absorption mismatch (as discussed in § 3.2), and the  $\kappa_0 v^2 E/c$  as the “relativistic work” arising from the relativistic flux. The presence or absence of this relativistic work term is the difference between our leading order-accurate equation and the equation one would derive by dropping  $\beta^2$  terms. Analyzing when, if ever, this term is physically important lets us identify in which situations a lower order treatment may be inadequate.

If we use Table 2 to compare the relativistic work term to the emission/absorption term, we find that  $(\kappa_0 v^2 E/c)/[\kappa_0(4\pi B - cE)]$  is of order  $\beta^2 \tau^2$  for static diffusion, and of

order unity for dynamic diffusion. Thus, the term is never important in a static diffusion problem, but is always important for a non-uniform, non-equilibrium dynamic diffusion problem system. We expect any system where variations occur on a scale for which  $\beta\tau \gg 1$  to resemble a uniform, equilibrium medium, and thus we do not expect the term  $(4/3)\kappa_0 v^2 E/c$  to be important in such a system.

That said, there is still clearly a problem with omitting the relativistic work term in a system where  $\beta\tau \sim 1$ . In this case, Table 2 implies that *every* term on the right hand side is roughly equally important regardless of whether we use the static or dynamic diffusion scalings. We have shown (Krumholz *et al.*(2007b)) that one can obtain the correct structure within a radiation-dominated shock only by retaining the relativistic work term.

An interesting point to note here is that omitting the relativistic work term will not produce errors upstream or downstream of a shock, because  $\beta\tau \gg 1$  in these regions. The omitted term will however affect radiation-gas energy exchange, not total energy conservation. The lower order treatment will therefore only make errors within the shock. Whether this is physically important depends on whether one is concerned with structures on scales for which  $\beta\tau \sim 1$ . An astrophysical example of a system where one does care about structures on this scale is a radiation-dominated accretion disk subject to photon bubble instability (Turner *et al.* (2003)). Such disks are in the dynamic diffusion regime over the entire disk, but photon bubbles form on small scales within them, and individual bubbles may have  $\beta\tau \sim 1$  across them.

### 3.3.2. Comparison to Comoving Frame Formulations

Many popular numerical treatments of radiation hydrodynamics (Turner & Stone(2001), Whitehouse & Bate(2004), Hayes *et. al.* (2006)) use a comoving formulation of the equations rather than our mixed frame formulation. It is therefore useful to compare our equations to the standard comoving frame equations. In the comoving formulation, the evolution equation for the radiation field is usually the first law of thermodynamics for the comoving radiation field as shown by Mihalas & Klein(1982),

$$\rho \frac{D}{Dt} \left( \frac{E_0}{\rho} \right) + \mathcal{P}_0 : (\nabla \mathbf{v}) = \kappa_0 (4\pi B - cE_0) - \nabla \cdot \mathbf{F}_0. \quad (3.35)$$

This equation is accurate to first order in  $\beta$  in the sense that it contains all the correct leading order terms and all terms that are smaller than them by order  $\beta$  or less.

To compare this to our mixed frame radiation energy equation (3.32), we replace the comoving frame energy  $E_0$  in (3.35) with the lab frame energy  $E$  using the Lorentz transformation Mihalas & Weibel-Mihalas(1999) and retain all terms that are of leading order in any regime. This gives a transformed equation

$$\begin{aligned} \rho \frac{D}{Dt} \left( \frac{E}{\rho} \right) + \mathcal{P}_0 : (\nabla \mathbf{v}) &= \kappa_0 (4\pi B - cE) - \nabla \cdot \mathbf{F}_0 \\ &+ 2\kappa_0 \frac{\mathbf{v} \cdot \mathbf{F}_0}{c} + \frac{\kappa_0}{c} [v^2 E + (\mathbf{v}\mathbf{v}) : \mathcal{P}_0]. \end{aligned} \quad (3.36)$$

If we now adopt the diffusion approximation  $\mathbf{F}_0 = -c/(3\kappa_0)\nabla E_0$  and  $\mathcal{P}_0 = (1/3)E_0\mathcal{I}$ , use the Lorentz transformation to replace  $E_0$  with  $E$  throughout, and again only retain terms that are of leading in order in some regime, then it is easy to verify that (3.36) reduces to (3.33). Thus, our evolution equation is equivalent to the comoving frame first law of thermodynamics for the radiation field, *provided that one retains all the leading order terms with respect to  $\beta$  and  $\tau$ , including some that are of order  $\beta^2$ , when evaluating the Lorentz transformation.*

While the equations are equivalent, the mixed frame formulation has two important advantages over the comoving frame formulation when it comes to practical computation. First, we are able to write the equations in a manner that allows a numerical solution algorithm to conserve total energy to machine accuracy. We present such an algorithm in Krumholz *et al.* (2007b). In contrast, it is not possible to write a conservative update algorithm using the comoving frame equations. The reason for this is that a conserved total energy only exists in an inertial frame, and for a fluid whose velocity is not a constant in space and time, the comoving frame is not inertial. The lack of a conserved energy is a serious drawback to comoving frame formulations.

A second advantage of the mixed-frame formulation is that it is far more suited to implementation in codes with dynamically modified grid structures such as adaptive mesh refinement methods. Since the radiation energy is a conserved quantity, it is obvious how to refine or coarsen it in a conservative manner. On the other hand, there is no obviously correct method for refining or coarsening the comoving frame energy density, because it will not even be defined in the same reference frames before and after the refinement procedure.

### 3.4. Radiation Hydrodynamics in the Static Diffusion Limit

Our analysis shows that for static diffusion, the terms involving diffusion and emission minus absorption of radiation always dominate over those involving radiation work and advection. In addition, some terms are always smaller than order  $\beta$ . This suggests an opportunity for a significant algorithmic improvement over earlier approaches while still retaining order  $\beta$  accuracy in the solution. In a simulation, one must update terms for the radiation field implicitly, because otherwise stability requirements limit the update time step to values comparable to the light-crossing time of a cell. Standard approaches (e.g. Turner & Stone(2001), Whitehouse & Bate(2004), Whitehouse *et al.*(2005), Hayes *et al.*(2006)) therefore update all terms involving radiation implicitly except the advection term and the radiation force term in the gas momentum equation.

However, implicit updates are computationally expensive, so the simpler the terms to be updated implicitly can be made, the simpler the algorithm will be to code and the faster it will run. Since the work and advection terms are non-dominant, we can produce a perfectly stable algorithm without treating them implicitly. Even if this treatment introduces numerically unstable modes in the work or advection terms, they will not grow because the radiation diffusion and emission/absorption terms, which are far larger, will smooth them away each time step.

For the case of static diffusion, we therefore adopt the order  $v/c$  equations (3.6) and (3.30) for mass and momentum conservation. For our energy equations, we adopt (3.31) and (3.32), but drop terms that are smaller than order  $\beta$  for static diffusion. This gives

$$\begin{aligned} \frac{\partial}{\partial t}(\rho e) = & -\nabla[(\rho e + P)\mathbf{v}] - \kappa_{0P}(4\pi B - cE) \\ & + \lambda \left( 2 \frac{\kappa_{0P}}{\kappa_{0R}} - 1 \right) \mathbf{v} \cdot \nabla E \end{aligned} \quad (3.37)$$

$$\begin{aligned} \frac{\partial}{\partial t} E = & \nabla \cdot \left( \frac{c\lambda}{\kappa_{0R}} \nabla E \right) + \kappa_{0P}(4\pi B - cE) \\ & - \lambda \left( 2 \frac{\kappa_{0P}}{\kappa_{0R}} - 1 \right) \mathbf{v} \cdot \nabla E \\ & - \nabla \cdot \left( \frac{3 - R_2}{2} \mathbf{v} E \right) \end{aligned} \quad (3.38)$$

To solve these, we operator split the diffusion and emission/absorption terms, which we treat implicitly, from the work and advection terms, which we treat explicitly. For each update cycle, we start with the state at the old time. We first perform an implicit update to the radiation and gas energy densities using radiative terms that are handled implicitly. For our implementation of this algorithm in the Orion adaptive mesh refinement (AMR) code, we use the method of Howell & Greenough(2003), which we will not discuss in detail here. To summarize, the algorithm involves writing the equations using second order accurate spatial discretization and a time discretization that limits to backwards Euler for large values of  $\partial E/\partial t$  (to guarantee stability) and to Crank-Nicolson when  $\partial E/\partial t$  is small (to achieve second order time accuracy). This yields a matrix equation for the radiation and gas energy densities at the new time, which may be solved on both individual grids and over a hierarchy of nested grids (as is necessary for AMR) using standard multigrid techniques. The output of this procedure is an intermediate state which has been updated for the implicit terms.

Once the implicit update is done, we compute the ordinary hydrodynamic update. As with the implicit update, this may be done using the hydrodynamics method of one's choice. For our implementation, we use the Godunov method described by Truelove *et al.*(1998), Klein (1999), and Fisher (2002). This update gives us a state updated for implicit radiative terms and explicit non-radiative terms.

Finally, we explicitly compute the radiative force and advection terms and then find the new state at the advanced time

This update is manifestly only first order-accurate in time for the explicit radiation terms, but there is no point in using a more complex update because our operator splitting of some of the radiation terms means that we are performing our explicit update using a time-advanced radiation field, rather than the field at a half time step. Truelove *et al.*(1998) show that one can avoid this problem for gravitational body forces because the potential is linear in the density, so it is possible to derive the half-time step potential from the whole time step states. No such fortuitous coincidence occurs for the radiation field. This necessarily limits us to first order accuracy in time for the terms we treat explicitly. However, since these terms are always small compared to the dominant radiation terms, the overall scheme should still be closer to second order than first order in accuracy.

### 3.5. *Advantages of the Method*

Our algorithm has two significant advantages in comparison to other approaches, in particular those based on comoving frame formulations of the equations (Turner & Stone(2001), Whitehouse *et al.*(2005), Hayes *et al.*(2006)). In any of these approaches, since the radiation work terms are included in the implicit update, one must solve an implicit quartic equation arising from the combination of the terms  $\kappa_{0P}(4\pi B - cE)$  and  $\mathcal{P}:\nabla\mathbf{v}$ . This may be done either at the same time one is iterating to update the flux divergence term  $\nabla\cdot\mathbf{F}$  (Whitehouse *et al.*(2005)), or in a separate iteration to be done once the iterative solve for the flux divergence update is complete (Turner & Stone(2001), Hayes *et al.*(2006)). In contrast, since our iterative update involves only  $\kappa_{0P}(4\pi B - cE)$  and  $\nabla\cdot\mathbf{F}$ , using the Howell & Greenough(2003) algorithm we may linearize the equations and never need to solve a quartic, leading to a simpler update algorithm and a faster iteration step. Moreover, by using the Howell & Greenough(2003) time-centering, we obtain second order accuracy in time whenever  $E$  is changing slowly, as opposed to the backwards Euler differencing of Turner & Stone(2001), Whitehouse *et al.* (2005), and Hayes *et al.* (2006), which is always first order-accurate in time. Thus, our algorithm provides a faster and simpler approach than the standard one.

A second advantage of our update scheme is that it retains the total energy-conserving character of the underlying equations. In each of the update steps involving radiation, for  $\mathbf{f}_{e-\text{rad}}$  and  $\mathbf{f}_i$ , the non-advective update terms in the radiation and gas energy equations are equal and opposite. Thus, it is trivial to write the update scheme so that it conserves total energy to machine precision. This property is particularly important for turbulent flows with large radiation energy gradients, such as those that occur in massive star formation (Krumholz *et al.*(2007a)), because numerical non-conservation is likely to be exacerbated by the presence of these features. In contrast, in comoving frame formalisms such as those of Turner & Stone(2001), Whitehouse & Bate(2004), and Hayes *et al.*(2006) the exchange terms in their gas and radiation energy equations are not symmetric. As a result, their update schemes do not conserve total energy exactly. The underlying physical reason for this asymmetry is that total energy is conserved only in inertial frames such as the lab frame; it is not conserved in the non-inertial comoving frame. For this reason, there is no easy way to write a conservative update scheme from a comoving formulation.

For dynamic diffusion problems, e.g. stellar interiors or radiation-dominated shocks, the work and advection terms can be comparable to or larger than the diffusion and heating/cooling terms and an algorithm that treats all the terms implicitly may be required.

The subtle limitation is in our treatment of the hydrodynamics. We perform the hydrodynamic update using a Riemann solver unmodified for the presence of radiation force, work, and heating and cooling terms. These terms should change the characteristic velocities of the wave families in ways that depend on the radiation hydrodynamic regime of the system. The severity of these effects for a given problem depends the degree of stiffness of the radiation source terms.

### 3.6. Tests in the Optically Thin and Thick Limits

As we have previously shown with MHD, strong tests of the coupling of the radiation with the hydrodynamics are crucial for gaining insight to different numerical approaches. Here we describe three tests of our radiation hydrodynamic algorithm, done using our implementation of the algorithms in the Orion AMR code whose different components are described in detail by Truelove *et al.*(1998), Klein (1999), Fisher (2002), and Crockett *et al.* (2005). For all of these tests we use a single fluid with no magnetic fields and no self-gravity. We describe additional tests in Krumholz *et al.* (2007b).

#### 3.6.1. Radiating Blast Wave

We first compare to a test problem in which the gas is not at rest: a Sedov-type blast wave with radiation diffusion. Reinicke & Meyer-ter-Vehn(1991) gave the first similarity solution to the problem of a point explosion with heat conduction, and following Sheshtakov(1999) and Sheshtakov & Greenough(2001), we can adapt this solution to the case of a point explosion with radiation diffusion. This tests our code's ability to follow coupled radiation-hydrodynamics in cases where radiation pressure is small.

We first summarize the semi-analytic solution. Consider an  $n = 3$  dimensional space filled with an adiabatic gas with equation of state  $P = (\gamma - 1)\rho e \equiv \Gamma\rho T$ , where  $\Gamma$  is the gas constant. The Planck mean opacity  $\kappa_{0P}$  of the gas is very high, so the gas and radiation temperatures are always equal. The Rosseland mean opacity has a powerlaw form  $\kappa_{0R} = \kappa_{0R,0}\rho^m T^{-n}$ , and we assume that it is always high enough to place us in the diffusion regime, so  $\lambda = 1/3$ . Note that the choice of  $-n = -3$  as the exponent of the opacity powerlaw is a necessary condition for applying the Reinicke & Meyer-ter-Vehn(1991) conduction solution to our radiation diffusion problem. Moreover, the similarity solution does not include radiation energy density or pressure, so we consider



only temperatures for which the gas energy density and pressure greatly exceed the radiation energy density and pressure, i.e.  $\rho e \gg a_R T^4$ .

Under the assumptions described above, we may re-write the gas and radiation energy equations (3.31) and (3.32) as a single conduction-type equation for the temperature,

$$\rho c_v \frac{\partial}{\partial t} T = \nabla(\chi_0 \rho^a T^b \nabla T), \quad (3.39)$$

where  $c_v = \partial e / \partial T = \Gamma / (\gamma - 1)$  is the constant-volume specific heat of the gas,  $\chi_0 = 4ca_R / (3\kappa_{0R,0})$ ,  $a = -m$ , and  $b = n + 3$ . This equation has the same form as the conduction equation considered by Reinicke & Meyer-ter-Vehn(1991).

Consider now a point explosion at the origin of a spherically symmetric region with an initial powerlaw density distribution  $\rho(r, t = 0) = g_0 r^{-k_\rho}$ . Initially the gas temperature  $T$  and pressure  $P$  are negligible. The explosion occurs at the origin at time zero, so the initial gas energy density is  $(\rho e)(r, t = 0) = E_0 \delta(\mathbf{r})$ . Reinicke & Meyer-ter-Vehn(1991) show that if the initial density profile has a powerlaw index

$$k_\rho = \frac{(2b - 1)n + 2}{2b - 2a + 1}, \quad (3.40)$$

then one may obtain a similarity solution via the change of variables

$$\xi = \frac{r}{\zeta t^\alpha} \quad (3.41)$$

$$G(\xi) = \frac{\rho(r, t)}{g_0 r^{-k_\rho}} \quad (3.42)$$

$$U(\xi) = v(r, t) \frac{t}{\alpha r} \quad (3.43)$$

$$\Theta(\xi) = T(r, t) \Gamma \left( \frac{\alpha r}{t} \right)^2. \quad (3.44)$$

Here,  $\xi$ ,  $G(\xi)$ ,  $U(\xi)$ , and  $\Theta(\xi)$  are the dimensionless distance, density, velocity, and temperature,

$$\alpha = \frac{2b - 2a + 1}{2b - (n + 2)a + n}, \quad (3.45)$$

and  $\zeta$  is a constant with units of [length][time] $^{-\alpha}$  whose value is determined by a procedure we discuss below.

With this similarity transformation, the equations of motion and heat conduction reduce to

$$U' - (1 - U)(\ln G)' + (n - k_\rho)U = 0 \quad (3.46)$$

$$(1 - U)U' + U(\alpha^{-1} - U) = \Theta[\ln(\xi^{2-k_\rho} G \Theta)]', \quad (3.47)$$

and

$$2[U' + nU - \mu(\alpha^{-1} - 1)] = \mu(1 - U)[\ln(\xi^2 \Theta)]' + \beta_0 \Theta^b G^{a-1} \xi^{(2b-1)/\alpha} \cdot ((\ln \Theta)'' + [\ln(\xi^2 \Theta)]') \quad (3.48)$$

$$\cdot \{n - 2 + a[\ln(\xi^{-k_\rho} G)]' + (b + 1)[\ln(\xi^2 \Theta)]'\}, \quad (3.49)$$

where  $()' \equiv d()/d \ln \xi$ ,  $\mu = 2/(\gamma - 1)$ , and

$$\beta_0 = \frac{2\chi_0(\alpha\zeta^{1/\alpha})^{2b-1}}{\Gamma^{b+1}g_0^{1-\alpha}} \text{sgn}(t). \quad (3.50)$$

This constitutes a fourth-order system of non-linear ordinary differential equations. All physical solutions to these equations pass through two discontinuities, a heat front and a shock front, with the heat front at larger radius. However, the jump conditions for these discontinuities are easy to determine, and one can integrate between them. For a given  $\beta_0$ , the solution depends only on the dimensionless parameter

$$\Omega = \frac{2\chi_0}{\Gamma^{b+1}g_0^{1-a}} \left( \frac{E_0}{g_0} \right)^{b-1/2}, \quad (3.51)$$

which measures the strength of the explosion. Large values of  $\Omega$  constitute “strong” explosions, and the ratio of heat front radius to shock front radius is a monotonically increasing function of  $\Omega$ . It is important at this point to add a cautionary note: in deriving the similarity solution, we assumed that radiation energy density is negligible in comparison to gas energy density. This cannot strictly be true at early times, since at  $t = 0$  the temperature diverges at the origin, and the radiation energy density varies as  $T$  to a higher power than the gas energy density. However, the true behavior should approach the similarity solution at later times.

While we have reduced the gas dynamical equations to a system of ordinary differential equations that is trivial to integrate, solving the full problem is complex because the equations still depend on the unknown parameter  $\beta_0$ , which in turn depends on  $\zeta$ . To solve the problem, we must determine  $\beta_0$  from the given initial conditions. Reinicke & Meyer-ter-Vehn(1991) describe the iteration procedure required to do this in detail, and we only summarize it here. To find a solution, one first chooses a value  $\xi_h > 1$  for the dimensionless radius of the heat front, applies the boundary conditions at the front, and guesses a corresponding value of  $\beta_0$ . For each  $\xi_h$  there exists a unique  $\beta_0$  for which it is possible to integrate the equations back from  $\xi = \xi_h$  to the location of the shock front at  $\xi = \xi_s$ , apply the shock jump conditions, and continue integrating back to the origin at  $\xi = 0$  without having the solution become double-valued and thus unphysical. One iterates to identify the allowed value of  $\beta_0$  for the chosen  $\xi_h$ , and this gives the unique density, velocity, and temperature profiles allowed for that  $\xi_h$ . However, the solution one finds in this way may not correspond to the desired value of  $\Omega$ . Reinicke & Meyer-ter-Vehn(1991) show that

$$\Omega = \beta_0 \left[ 2\pi \int_0^{\xi_h} \xi^{n-k_\rho+1} G(U^2 + \mu\Theta) d\xi \right]^{b-1/2}. \quad (3.52)$$

Thus, each choice of  $\xi_h$  corresponds to a particular value of  $\Omega$ , and one must iterate a second time to find the value of  $\xi_h$  that gives the value of  $\Omega$  determined from the input physical parameters of the problem. Alternately, instead of specifying a desired value of  $\Omega$ , one may specify a ratio  $R = \xi_h/\xi_s$ , which also determines a unique value for  $\xi_h$ .

For our comparison between the semi-analytic solution and Orion, we adopt the parameters  $\gamma = 7/5$ ,  $c_v = 1/(\gamma-1)$ ,  $a = -2$ ,  $b = 6$ ,  $g_0 = \chi_0 = 1$ , and  $E_0 = 135$ , which yields a strength  $\Omega = 1.042 \times 10^{12}$  and a ratio  $R = 2.16$ . In the simulation, we turn off terms in the code involving radiation pressure and forces, and we set  $\lambda = 1/3$  exactly. We use one-dimensional spherical polar coordinates rather than Cartesian coordinates; the solution procedures for this are identical to the ones outlined in § 3.4, with the exception that the gradient and divergence operators have their spherical rather than Cartesian forms, and the cell-centered finite differences are modified appropriately. Our computational domain goes covers  $0 \leq r \leq 1.05$ , resolved by 256, 512, or 1024 cells, and has reflecting inner and outer boundary conditions. To initialize the problem we set initial density to the powerlaw profile  $\rho = r^{-k_\rho}$  (with  $k_\rho$  set from equation 3.40), the initial velocity to zero,

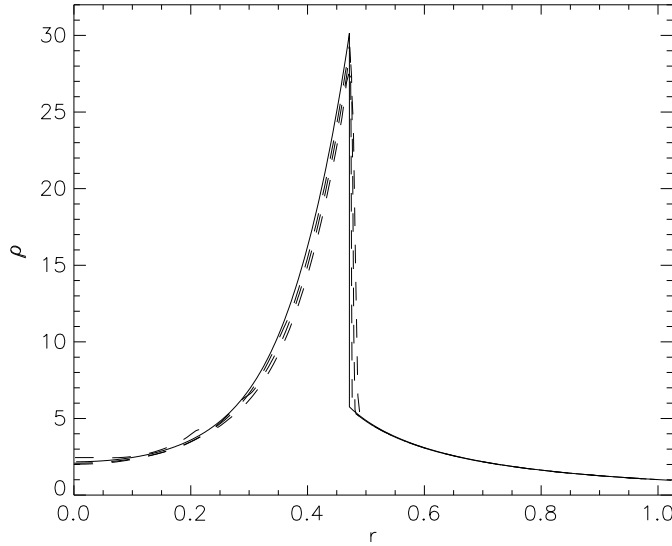


FIGURE 6. Density  $\rho$  versus radius  $r$  for the radiating blast wave test. We show the semi-analytic solution (*solid line*), and the Orion results at resolutions of 256, 512, and 1024 cells (*dashed lines*). The 256-cell run is the dashed line furthest from the semi-analytic solution, and the 1024-cell run is the dashed line closest to it.

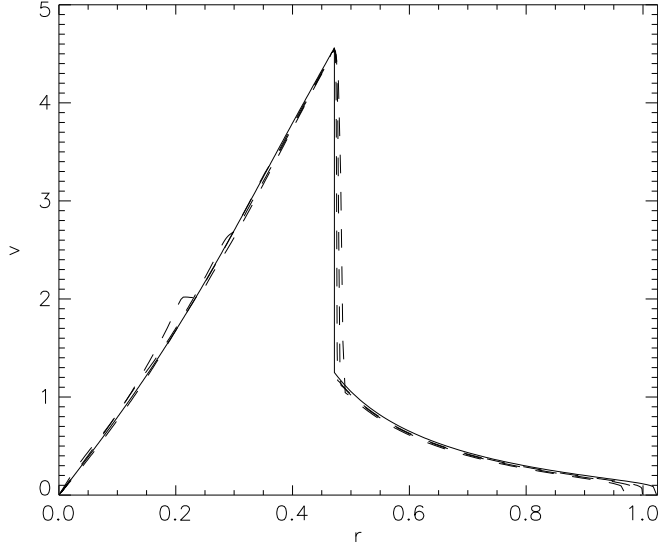
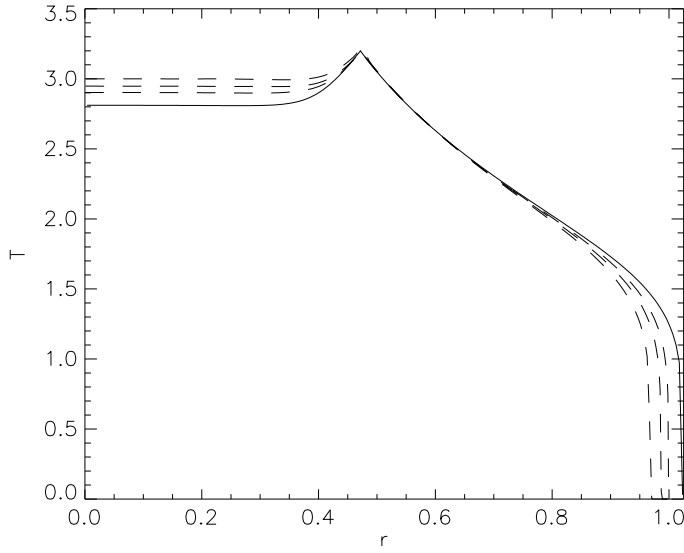
and the initial energy density to a small value, except in the cell adjacent to the origin, where its value is  $\rho e = 135/(\gamma - 1)$ .

Figures 6, 7, and 8 compare the semi-analytic density, velocity, and temperature profiles to the values we obtain from Orion after running to a time  $t = 0.06$ . As the plots show, the Orion results agree very well with the semi-analytic solution, and the agreement improves with increasing resolution. In the lowest resolution run, there is a small oscillation in the density and velocity about a third of the way to the shock, which is likely due to the initial blast energy being deposited in a finite-volume region rather than as a true  $\delta$  function. However, this vanishes at higher resolutions. Overall, the largest errors are in the temperature in the shocked gas.

As a metric of convergence, we plot the error of our simulation relative to the analytic solution as a function of resolution in Figure 9. We do this for the quantities  $r_h$  and  $r_s$ , the positions of the shock and heat fronts, and their ratio  $R$ . For this purpose, we define the location of the heat and shock fronts for the simulations as the positions of the cell edges where  $dT/dr$  and  $d\rho/dr$  are most negative. As the plot shows, at the highest resolution the errors in all three quantities are  $\lesssim 3\%$ , and the calculation appears to be converging. The order of convergence is roughly 0.6 in all three quantities. It is worth noting that computing the locations of the heat and shock fronts is a particularly strong code test, because obtaining the correct propagation velocities for the two fronts requires that the code conserve total energy very well. Non-conservative codes have significant difficulties with this test (e.g. Timmes *et al.* (2006)).

### 3.6.2. Radiation Pressure Tube

Our second test is to simulate a tube filled with radiation and gas. The gas within the tube is optically thick, so the diffusion approximation applies. The two ends of the tube are held at fixed radiation and gas temperature, and radiation diffuses through the gas

FIGURE 7. Same as Figure 6, but for the velocity  $v$ .FIGURE 8. Same as Figure 6, but for the temperature  $T$ .

from one end of the tube to the other. The radiation flowing through the tube exerts a force on the gas, and the gas density profile is such that, with radiation pressure, the gas is in pressure balance and should be stationary. For computational simplicity, we set the Rosseland- and Planck-mean opacities per unit mass of the gas to a constant value  $\kappa$ . A simulation of this system tests our code's ability to compute accurately the radiation pressure force in the very optically thick limit.

We first derive a semi-analytic solution for the configuration of the tube satisfying our desired conditions. Since the gas is very optically thick and we are starting the system

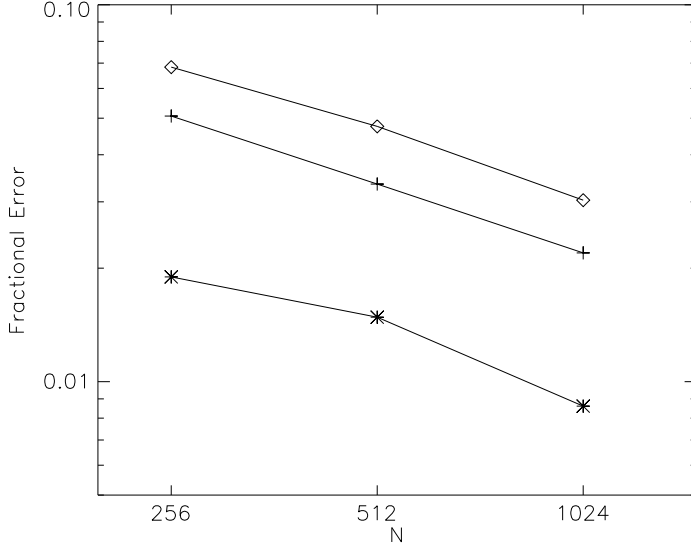


FIGURE 9. Fractional error versus resolution  $N$  in the radiating blast wave test. The fractional error is defined as  $|\text{simulation value} - \text{analytic value}|/\text{analytic value}$ . We show error in the heat front radius  $r_h$  (*plus signs*), shock front radius  $r_s$  (*asterisks*), and their ratio  $R = r_h/r_s$  (*diamonds*).

in equilibrium, we set  $T_{\text{rad}} = T_{\text{gas}} \equiv T$ . The fluid is initially at rest. The condition of pressure balance amounts to setting  $\partial(\rho\mathbf{v})/\partial t + \nabla \cdot (\rho\mathbf{v}\mathbf{v}) = 0$  in equation (3.30), so that the radiation pressure force balances the gas pressure gradient. Thus, we have

$$\frac{dP}{dx} + \lambda \frac{dE}{dx} = 0 \quad (3.53)$$

$$\left( \frac{k_B}{\mu} \rho + \frac{4}{3} a_R T^3 \right) \frac{dT}{dx} + \frac{k_B}{\mu} T \frac{d\rho}{dx} = 0. \quad (3.54)$$

In the second step we have set  $E = a_R T^4$  and  $P = \rho k_B T / \mu$ , where  $\mu$  is the mean particle mass, and we have set  $\lambda = 1/3$  as is appropriate for the optically thick limit. The radiation energy equation (3.38) for our configuration is simply

$$\frac{d}{dx} \left( \frac{c\lambda}{\kappa\rho} \frac{dE}{dx} \right) = 0 \quad (3.55)$$

$$\frac{d^2 T}{dx^2} + 3 \frac{1}{T} \left( \frac{dT}{dx} \right)^2 - \frac{1}{\rho} \left( \frac{d\rho}{dx} \right) \left( \frac{dT}{dx} \right) = 0. \quad (3.56)$$

Equations (3.54) and (3.56) are a pair of coupled non-linear ordinary differential equations for  $T$  and  $\rho$ . The combined degree of the system is three, so we need three initial conditions to solve them. Thus, let the tube run from  $x = x_0$  to  $x = x_1$ , with temperature, density, and density gradient  $T_0$ ,  $\rho_0$ , and  $(d\rho/dx)_0$  at  $x_0$ . For a given choice of initial conditions, it is trivial to solve (3.54) and (3.56) numerically to find the density and temperature profile. We wish to investigate both the radiation pressure and gas pressure dominated regimes, so we choose parameters to ensure that our problem covers both. The choice  $x_0 = 0$ ,  $x_1 = 128$  cm,  $\rho_0 = 1$  g cm $^{-3}$ ,  $(d\rho/dx)_0 = 5 \times 10^{-3}$  g cm $^{-4}$ , and  $T_0 = 2.75 \times 10^7$  K satisfies this requirement if we adopt  $\mu = 2.33 m_P = 3.9 \times 10^{-24}$  g and

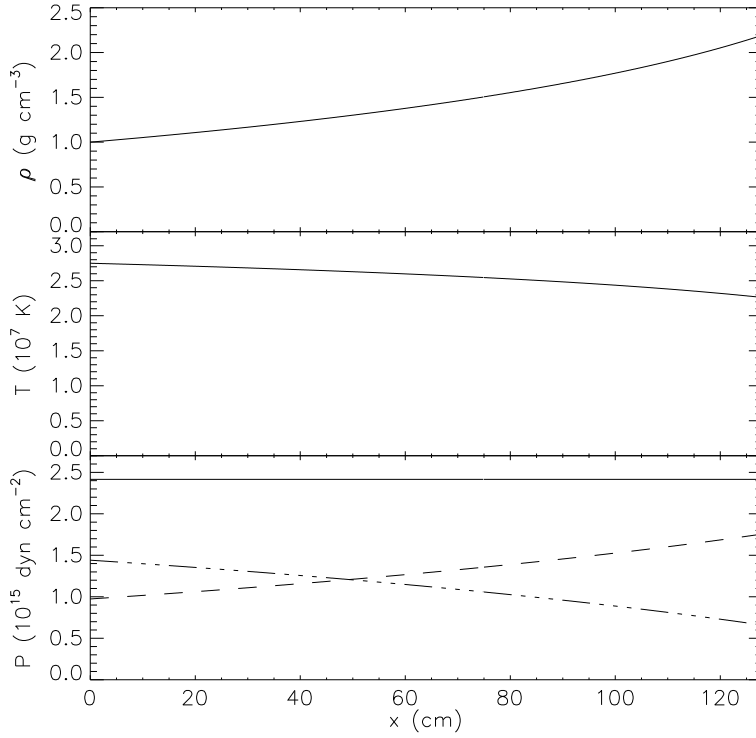


FIGURE 10. Density, temperature, and pressure versus position in the radiation tube problem. The bottom panel shows total pressure (*solid line*), gas pressure (*dashed line*), and radiation pressure (*dot-dashed line*).

$\kappa = 100 \text{ cm}^2 \text{ g}^{-1}$ . Figure 10 shows the density, temperature, and pressure as a function of position for these parameters.

We solve the equations to obtain the density and temperature as a function of position, and then set these values as initial conditions in a simulation. The simulation has 128 cells along the length of the tube on the coarsest level. We impose Dirichlet boundary conditions on the radiation field, with the radiation temperature at each end of the tube set equal to its value as determined from the analytic solution. We use symmetry boundary conditions on the hydrodynamics, so that gas can neither enter nor leave the computational domain. To ensure that our algorithm does not encounter problems at the boundaries between AMR levels, we refine the central 1/4 of the problem domain to double the resolution of the base grid. We evolve the system for 10 sound crossing times and measure the amount by which the density and temperature change relative to the exact solution. We plot the relative error, defined as  $(\text{numerical solution} - \text{analytic solution}) / (\text{analytic solution})$ , in the density, gas temperature, and radiation temperature in Figure 11. As the plot shows, our numerical solution agrees with the analytic result to better than 0.5% throughout the computational domain. The density error is smallest in the higher resolution central region, as expected. There is a very small increase in error at level boundaries, but it is still at the less than 0.5% level.

### 3.6.3. Radiation-Inhibited Bondi Accretion

The previous test focuses on radiation pressure forces in the optically thick limit. To test the optically thin limit, we simulate accretion onto a radiating point particle.

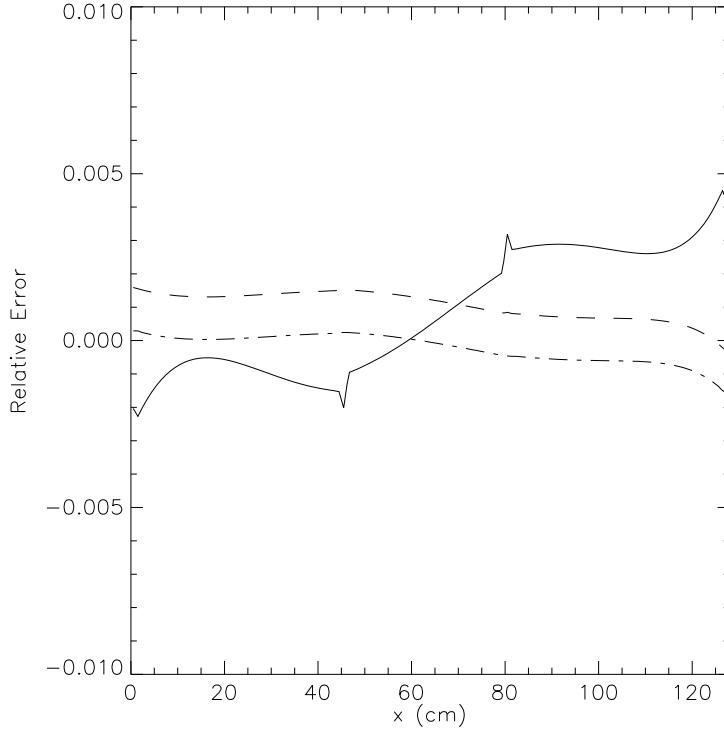


FIGURE 11. Relative error in density (*solid line*), gas temperature (*dashed line*), and radiation temperature (*dot-dashed line*) in the radiation tube test.

We consider a point mass  $M$  radiating with a constant luminosity  $L$  accreting from a background medium. The medium consists of gas which has zero velocity and density  $\rho_\infty$  far from the particle. We take the gas to be isothermal with constant temperature  $T$ , and enforce that it is not heated or cooled radiatively by setting its Planck opacity  $\kappa_{0P} = 0$ . We set the Rosseland opacity of the gas to a constant non-zero value  $\kappa_{0R}$ , and choose  $\rho_\infty$  such that the computational domain is optically thin. In this case, the radiation free-streams away from the point mass, and the radiation energy density and radiative force per unit mass on the gas are

$$E = \frac{L}{4\pi r^2 c} \quad (3.57)$$

$$\mathbf{f}_r = \frac{\kappa_{0R} L}{4\pi r^2 c} \left( \frac{\mathbf{r}}{r} \right), \quad (3.58)$$

where  $\mathbf{r}$  is the radial vector from the particle and  $r$  is its magnitude. The gravitational force per unit mass is  $\mathbf{f}_g = -(GM/r^2)(\mathbf{r}/r)$ , so the net force per unit mass is

$$\mathbf{f} = \mathbf{f}_r + \mathbf{f}_g = -(1 - f_{\text{Edd}}) \frac{GM}{r^2} \left( \frac{\mathbf{r}}{r} \right), \quad (3.59)$$

where

$$f_{\text{Edd}} = \frac{\kappa_{0R} L}{4\pi GM c} \quad (3.60)$$

is the fraction of the Eddington luminosity with which the point mass is radiating.

Since the addition of radiation does not alter the  $1/r^2$  dependence of the specific force,

the solution is simply the standard Bondi(1952) solution, but for an effective mass of  $(1 - f_{\text{Edd}})M$ . The accretion rate is the Bondi rate

$$\dot{M}_B = 4\pi\xi r_B^2 c_s \rho_\infty, \quad (3.61)$$

where

$$r_B = (1 - f_{\text{Edd}}) \frac{GM}{c_s^2} \quad (3.62)$$

is the Bondi radius for the effective mass,  $c_s$  is the gas sound speed at infinity, and  $\xi$  is a numerical factor of order unity that depends on the gas equation of state. For an isothermal gas,  $\xi = e^{3/2}/4$ , and the radial profiles of the non-dimensional density  $\alpha \equiv \rho/\rho_\infty$  and velocity  $u \equiv v/c_s$  are given by the solutions to the non-linear algebraic equations Shu(1992)

$$x^2 \alpha u = \xi \quad (3.63)$$

$$\frac{u^2}{2} + \ln \alpha - \frac{1}{x} = 0, \quad (3.64)$$

where  $x \equiv r/r_B$  is the dimensionless radius.

To set up this test, we make use of the Lagrangian sink particle algorithm of Krumholz *et al.* (2004), coupled with the “star particle” algorithm of Krumholz *et al.* (2007a) which allows the sink particle to act as a source of radiation. We simulate a computational domain  $5 \times 10^{13}$  cm on a side, resolved by  $256^3$  cells, with a particle of mass  $M = 10 M_\odot$  and luminosity  $L = 1.6 \times 10^5 L_\odot$  at its center. We adopt fluid properties  $\rho_\infty = 10^{-18}$  g cm $^{-3}$ ,  $\kappa_{\text{OR}} = 0.4$  cm $^2$  g $^{-1}$ , and  $c_s = 1.3 \times 10^7$  cm s $^{-1}$ , corresponding to a gas of pure, ionized hydrogen with a temperature of  $10^6$  K. With these values,  $f_{\text{Edd}} = 0.5$ ,  $r_B = 4.0 \times 10^{12}$  cm, and  $\dot{M}_B = 2.9 \times 10^{17}$  g s $^{-1}$ . We use inflow boundary conditions on the gas and Dirichlet boundary conditions on the radiation field, with the radiation energy density on the boundary set to the value given by equation (3.57).

Figure 12 compares the steady-state density  $\alpha$  and velocity  $u$  computed by Orion to the analytic solution. The agreement is excellent, with differences between the analytic and numerical solutions of  $\sim 1\%$  everywhere except very near the accretion radius at  $x = 0.25$ . The maximum error is  $\sim 10\%$  at the surface of the accretion region; this is comparable to the error in density for non-radiative Bondi accretion with similar resolution in Krumholz *et al.* (2004). In comparison, the solution is nowhere near the solution that would be obtained without radiation. After running for 5 Bondi times ( $= r_B/c_s$ ), the average accretion rate is  $2.4 \times 10^{17}$  g s $^{-1}$ . While this differs from the analytic solution by 19%, the error is also not tremendously different from that obtained by Krumholz *et al.* (2004) when the Bondi radius was resolved by 4 accretion radii, and is nowhere near the value of  $1.2 \times 10^{18}$  g s $^{-1}$  which would occur without radiation.

We should at this point mention one limitation of our algorithm, as applied on an adaptive grid, that this test reveals. The  $1/r^2$  gradient in the radiation energy density is very steep, and we compute the radiation force by computing gradients in  $E$ . We found that, in an AMR calculation, differencing this steep gradient across level boundaries introduced significant artifacts in the radiation pressure force. With such a steep gradient, we were only able to compute the radiation pressure force accurately on fixed grids, not adaptive grids. This is not a significant limitation for most applications though, since for any appreciable optical depth the gradient will be much shallower than  $1/r^2$ . As the radiation pressure tube test in § 3.6.2 demonstrates, in an optically thick problem the errors that arise from differencing across level boundaries are less than 1%.



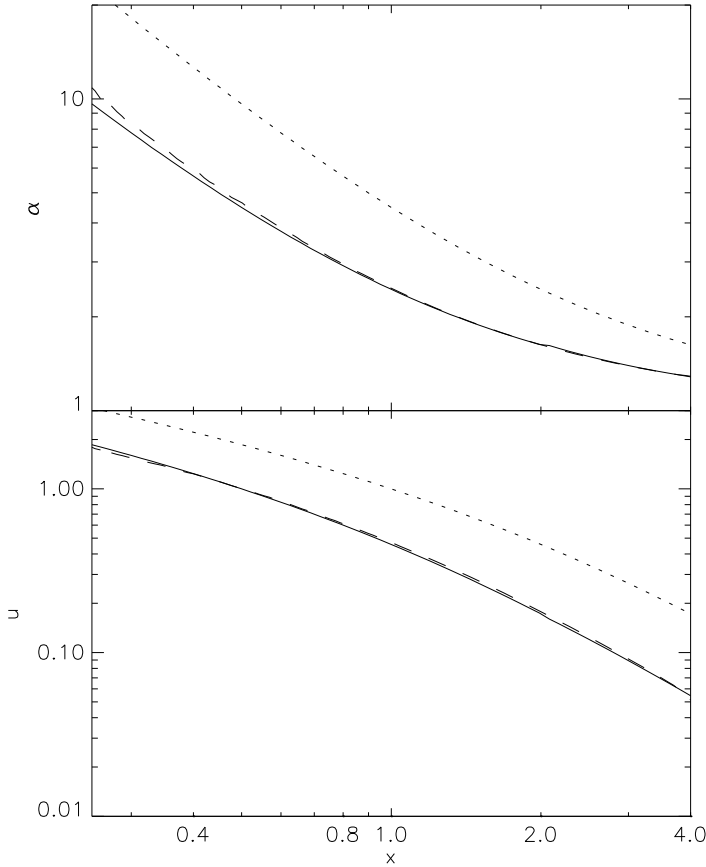


FIGURE 12. Dimensionless density  $\alpha$  (*upper panel*) and velocity  $u$  (*lower panel*) versus dimensionless position  $x$  for radiation-inhibited Bondi accretion. We show the analytic solution (*solid line*), the solution as computed with Orion (*dashed line*), and the analytic solution for Bondi accretion without radiation (*dotted line*). For the Orion result, the values shown are the radial averages computed in 128 logarithmically-spaced bins running from the accretion radius  $x = 0.25$  to the outer edge of the computational domain  $x = 5$ .

#### 4. Adaptive Mesh Refinement

The numerical algorithm used for radiation hydrodynamics in Orion and MHD in Athena is a high-resolution conservative finite-difference method for solving the compressible Euler equations. The basic finite volume method was a higher-order extension of Godunov's method. This algorithm is second-order accurate for smooth flow problems, and has a robust and accurate treatment of discontinuities. It has been used quite extensively to compute unsteady shock reflections in gases, and has a demonstrated ability to resolve complex interactions of discontinuities found in astrophysical flows and star formation Klein *et al.* (1994), Klein (1999)).

The supplementary technique employed in Orion to further enhance the efficiency and resolution of our calculations are local adaptive mesh refinement. The adaptive mesh refinement algorithm we employ, similar to Berger & Oliger(1984), is a dynamic regridding strategy based on an underlying rectangular discretization of the spatial domain.

The adaptive mesh refinement (AMR) scheme utilizes underlying rectangular grids at different levels of resolution. Linear resolution varies by integral refinement factors between levels, and a given grid is always fully contained within one at the next coarser level (excluding the coarsest grid). The AMR method dynamically resizes and repositions these grids and inserts new, finer ones within them according to adjustable refinement criteria, such as the numerical Jean's condition (Truelove *et al.* (1997)). Fine grids are automatically removed as flow conditions require less resolution. During the course of the calculation, some pointwise measure of the error is computed at frequent intervals – typically every other time step. At those times, the cells that are identified are covered by a relatively small number of rectangular patches, which are refined by some even integer factor. Refinement is in both time and space, so that the calculation on the refined grids is computed at the same CFL number as that on the coarse grid. This procedure is applied recursively, i.e. the error on the refined grid monitored, and the regions with large errors covered by refined rectangular patches. The overall algorithm is fully conservative: the finite difference approximations on each level are in conservation form, as is the coupling at the interface between grids at different levels of refinement.

There are several important features to this algorithm we wish to point out. The AMR uses a nested sequence of logically rectangular meshes to solve a PDE. In this work, we assume the domain is a single rectangular grid although it may be decomposed into several coarse grids. It is required that the discretized solution be independent of the particular decomposition of the domain into subgrids. Grids must be properly nested such that a fine grid should be at least one cell away from the boundary of the next coarser grid unless it is touching the boundary of the physical domain. However, a fine grid can cross a coarser grid boundary and still be properly nested. In this case, the fine grid has more than one parent grid.

AMR in Orion contains five separate components Klein (1999). The error estimation is used to estimate local truncation error. This determines where the solution is sufficiently accurate. The grid generator creates fine grid patches which cover the regions that need refinement. Data structure routines manage the grid hierarchy allowing access to the individual patches. Interpolation routines initialize a solution on a newly created fine grid and also provide the boundary conditions for integrating the fine grids. Flux correction routines ensure conservation at grid interfaces by modifying the coarse grid solution for coarse cells that are adjacent to a fine grid.

When all these components are assembled, a typical integration step proceeds as follows. The integration steps on different grids are interleaved so that before advancing a grid all the finer level grids have been integrated to the same time. One coarse grid cycle is then the basic unit of the algorithm. The mesh refinement factor in both space and time has been chosen most efficiently to be 4, although any even integer is possible. In practice we use as many levels of refinement above the base coarse grid level as is required by the physics of the calculation. The regridding procedure is done every few time steps. The updating of the data on the locally refined grid structure is organized around the grouping of cells into rectangular grid patches, each one of which typically containing several hundred to several thousand grid cells. For example, the AMR code passes to a subroutine a rectangular grid of dependent variables and precomputed values in a set of ghost cells surrounding the grid, and assumes that the subroutine updates the values in the rectangular grid by one time step, as well as passing back the fluxes at cell edges that had been used in the update. The overheads in both CPU and memory associated with the adaptive mesh structure have been kept quite small, relative to other irregular grid schemes. Typically, 80% - 90% of the total execution time is spent advancing cells in time using the finite difference code, while the memory required is that

needed to store two copies of the solution on all of the grids. These overheads are low because they are determined by the number of rectangles into which the AMR solution has been divided; as opposed to being determined by the number of grid cells, as is the case with the irregular grid adaptive algorithms.

In AMR, the computational volume consists of a hierarchical grid structure. A base Level 0 grid fills the computational volume, discretizing it on a rectangular grid with a resolution of  $\Delta x_0$  in each direction. Multiple Level 1 grids of finer resolution  $\Delta x_1 = \Delta x_0/r_1$  may be embedded within it, where  $r_1 = 4$  is a typical choice. In turn, multiple Level 2 grids of resolution  $\Delta x_2 = \Delta x_1/r_2$  may be embedded within Level 1, and so on. Grids at Level  $L$  always span an integral number of cells at Level  $L - 1$ , i.e., partial cell refinement is not permitted. Furthermore, a grid at Level  $L$  is always nested within a grid at Level  $L - 1$  such that there is a buffer region of Level  $L - 1$  cells surrounding it. In other words, a grid at Level  $L$  within a grid at Level  $L - 1$  never shares a boundary with the Level  $L - 1$  grid.

A key component of an AMR code is the procedure by which the decision is made whether or not a given portion of the flow is adequately resolved. In our code, this procedure is broken into two steps. In the first step, a specified property is measured in each cell, and the cell is flagged for refinement if a specified algorithm indicates the measurement requires it. In the second step, the distribution of cells requiring refinement is analyzed to determine the number, sizes, and locations of grids to be inserted at the next finer level of resolution. These finer grids will always include every cell that was flagged for refinement, but they may also include additional cells that were not flagged. The degree to which the refinement is concentrated in the cells that require it is termed the *grid efficiency*. The grid efficiency is minimal when the smallest rectangular solid containing all flagged cells is refined. In this case the fraction of refined volume actually containing cells that required refinement may be very small. The grid efficiency is maximal when the only cells refined are those that were flagged.

The MHD code Athena introduced in §2 also includes algorithms for local adaptive mesh refinement. The strategy and issues for implementation are largely identical to those discussed above for Orion, with only a few additional complications introduced by MHD. For instance, the prolongation and restriction operators required to interpolate solutions between fine and coarse meshes must obey the divergence-free constraint; we use the formulation due to Tóth & Roe (2002) in Athena. Secondly, the directionally unsplit CTU integration method used in Athena requires modification so that the divergence-free constraint is enforced during half-timestep (predict) steps in the algorithm. Several of the tests described in §2.8 have proved quite challenging for MHD AMR methods. In particular, advection of a field loop across a region of refined meshes can be most illuminating. If the divergence-free constraint is not satisfied a variety of effects can be noted, for example the loop shows distortions, or slices of the field components may show oscillations, or a planar field loop advected in the  $x - y$  plane in full 3D can anomalously show growth of  $B_z$ . A more complete discussion of some of these issues is given in Gardiner (2007). To conclude the discussion here, in Figure 13 we show an image of a passive contaminant from the evolution of an MHD Rayleigh Taylor instability computed on a 2D mesh with a base resolution of  $8 \times 16$  with 5 levels of refinement (the effective resolution of the finest grid is  $256 \times 512$ ). Initially the magnetic field is uniform and horizontal. Further details are given in Stone et al. (2007). The primary point here is that with careful attention to the divergence-free constraint, AMR methods for MHD based on CT can be designed which show no perturbations or anomalies in the field components at fine/coarse boundaries.

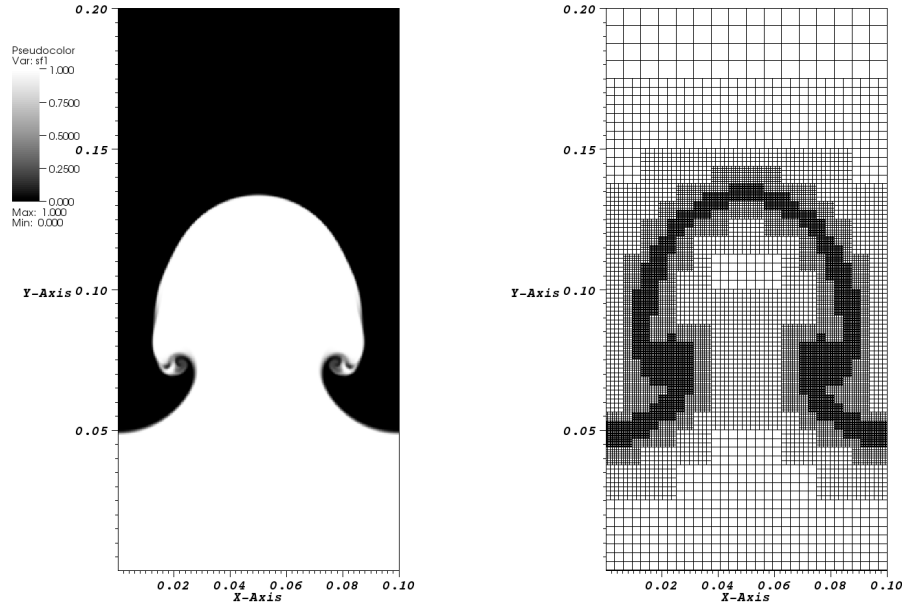


FIGURE 13. (*Left.*) Image of the a passive contaminant in a single mode MHD Rayleigh Taylor instability computed with an AMR version of Athena. (*Right.*) Grid distribution for the calculation.

## 5. Conclusions and Future Directions

We have described modern numerical algorithms for MHD and radiation hydrodynamics by focusing on the methods implemented in two separate codes: for MHD we have discussed Athena and for radiation hydrodynamics we have described the methods in Orion. Both codes continue to be developed in parallel directions. For example, Athena is being extended to radiation transport using variable Eddington tensors, while Orion has been extended to MHD using divergence-cleaning methods (Crockett *et al.* (2005)) and a constrained transport approach is being implemented as well.

In the future, significant advances in both algorithmic development as well as scalability and performance will be required to include all the relevant physics for star formation. For MHD, several robust and efficient algorithms seem to be available now. The focus is now turning to applications of high-order Godunov methods for MHD, including shearing-box studies of the MRI, and the properties of supersonic MHD turbulence. Extensions of the methods to non-ideal MHD, including finite resistivity and viscosity, is also important for studying, for example, protoplanetary disks.

For radiation hydrodynamics, Flux limited Diffusion as described here, already represents a significant advance over the use over the isothermal approximation or the barotropic stiffened equation of state approximation so widely used in star formation simulations. It also improves upon the Eddington approximation by suitable modification that compensates for errors made in dropping the time dependent flux term by including a correction factor in the diffusion coefficient for the radiation flux such that the flux goes to the diffusion limit at large optical depth and correct limits the flux to no larger than  $cE$  in the optically thin regime. Nevertheless, there are situations that can arise for

which optically thick structures that arise in marginally optically thin flow can present problems for Flux Limited Diffusion. Radiation flow that impinges upon optically thick structures in its path tends to fill in the region behind the opaque structure eventually immersing the structure in the radiation field rather than allowing the region to correctly form a shadow (Hayes & Norman (2003)). More accurate approaches such as Variable Eddington Tensors (Dykema *et al.* (1996)), Sn transport (Adams & Larsen (2002)) and Monte Carlo will be required. Although this situation can be improved by using an Eddington tensor moment approach, the shadow region still experiences moderate leakage of the radiation field after a few light crossing times (Hayes & Norman (2003)). Eddington tensors may also be costly with no guarantee of convergence.  $S_N$  methods and Monte Carlo methods are highly accurate and deal with the angle dependent transport equation directly. They have not yet been developed for simulations in star formation because the cost in 3D is prohibitive. The  $S_N$  method is a short characteristic method in which a bundle of rays is created at every mesh point and are extended in the upwind direction only as far as the next spatial cell. The main problem is in finding the efficient angle set to represent the radiation field in 2 or 3 dimensions (Castor, 2004). One might consider Monte Carlo methods to solve the transport equation. Although simple to implement (its great advantage), this method suffers from needing a vast number of operations per timestep to get accurate statistics in following the particles used to track the radiation field. Monte Carlo approaches however, may be extremely well parallelized and may make the best use of massively parallel platforms scaling up to petascale machines in the future. Both of these methods will however, avoid shadow effects and may be necessary to accurately treat optically thick inhomogeneous structures that form in accretion flows onto protostars. All of these approaches to radiation transport appear promising to us and are important to pursue in large scale simulations in the future. To achieve the huge dynamic range in scale posed by star formation, scaling to high numbers of processors (several  $\times 10^4$ ) will be necessary. Significant problems develop in load balancing issues (especially severe for AMR) for non-local physics. Strong coupling of non-local physics across the entire computational domain will require much more efficient parabolic and elliptic solvers for our algorithms. This too is a promising line of research for the future.

RIK thanks his collaborators Mark Krumholz, Robert Fisher and Christopher McKee for their contributions to the development of Orion. RIK is supported by NASA under NASA ATP grants NAG 5-12042 and NNG06GH96G ; the US Department of Energy at the Lawrence Livermore National Laboratory under contract W-7405-Eng-48; and the hospitality of KITP at Santa Barbara. RIK is also supported by grants of high performance computing resources from the NSF San Diego Supercomputer Center through NPACI program grant UCB267; the National Energy Research Scientific Computing Center, which is supported by the Office of Science of the U.S. Department of Energy under Contract No. DE-AC03-76SF00098, through ERCAP grant 80325; and the US Department of Energy at the Lawrence Livermore National Laboratory under contract W-7405-Eng-48.

JMS thanks Tom Gardiner, John Hawley and Peter Teuben for their contributions to the development of Athena. In particular, the AMR version of Athena described here is the work of Tom Gardiner. JMS is supported by the DOE through DE-FG52-06NA26217. Simulations were performed on the Teragrid cluster at NCSA, the IBM Blue Gene at Princeton University, and on computational facilities supported by NSF grant AST-0216105.

This work performed under the auspices of the U.S. Department of Energy by Lawrence Livermore National Laboratory under Contract DE-AC52-07NA27344.

## REFERENCES

- Adams, M. L. & Larsen, E. W. (2002), *Prog. Nucl. Energy*, **26**, 385.
- Alme, M. L. & Wilson, J. R. (1973), *Astrophys. J.*, **186**, 1015.
- Balsara, D.S., (1998) *Ap. J. Supp.*, 116, 133
- Balsara, D.S., (2001) *J. Comp. Phys.*, 174, 614.
- Balsara, D.S., & Spicer, D.S., (1999) *J. Comp. Phys.*, 149, 270
- Berger, M. J., & Olinger, J. (1984), *Journ. Comp. Phys.*, **53**, 484.
- Bondi, H. (1952), *Mon. Not. Roy Ast. Soc.*, **112**, 195.
- Cargo, P. & Gallice, G., (1997) *J. Comput. Phys.* **136**, 446
- Castor, J. I. (1972), *Astrophys. J.*, **178**, 779.
- (2004), *Radiation Hydrodynamics* (Cambridge, UK: Cambridge University Press).
- Colella, P., (1990) *J. Comp. Phys.*, 87, 171
- Colella, P. & Woodward, P.R., (1984) *J. Comput. Phys.* **54**, 174
- Crockett, R. K., Colella, P., Fisher, R. T., Klein, R. I., & McKee, C. F. (2005), *Journ. Comp. Phys.*, **203**, 422.
- Cunningham, A.J., Frank, A., Varniere, P., Mitran, S., & Jones, T.W., (2007), astro-ph:0710.0424
- Dai, W., & Woodward, P.R., (1994), *J. Comp. Phys.*, 1994, 115, 485
- Dai, W., & Woodward, P.R., (1998), *J. Comp. Phys.*, 1994, 142, 331
- Dedner, A., Kemm, F., Kröner, D., Munz, C.-T., Schnitzer, T., & Wesenberg, M., (2002) *J. Comp. Phys.*, 175, 645
- Dykema, P. G., Klein, R. I., & Castor, J. I. (1996), *Astrophys. J.*, **457**, 892.
- Evans, C.R. & Hawley, J.F., *Astrophys. J.* **322**, 659 (1988).
- Falle, S.A.E.G., Komissarov, S.S., & Joarder, P., (1998) *MNRAS*, 297, 265
- Fisher, R. T. (2002), PhD thesis, University of California, Berkeley.
- Fromang, S., Hennebelle, P., & Teyssier, R., 2006 *A&A*, 457, 371
- Gardiner, T., & Stone, J.M., 2005, *J. Comp. Phys.*, **205**, 509.
- Gardiner, T., & Stone, J.M., 2007, submitted to *J. Comp. Phys.*.
- Gardiner, T. (2007), to appear in proceedings of *ASTRONUM2007, 2nd International Conference on Numerical MOdeling of Space Plasma Flows*, AIP press.
- Hayes, J. C. & Norman, M. L. (2003), *Astrophys. J. Suppl.*, **147**, 197.
- Hayes, J. C., Norman, M. L., Fiedler, R. A., Bordner, J. O., Li, P. S., Clark, S. E., ud-Doula, A., & Mac Low, M.-M. (2006), *Astrophys. J. Suppl.*, **165**, 188.
- Howell, L. H. & Greenough, J. A. (2003), *Journ. Comp. Phys.*, **184**, 53.
- Hubeny, I. & Burrows, A. (2006), astro-ph/0609049.
- Kippenhahn, R. & Weigert, A. (1994), *Stellar Structure and Evolution* (Berlin: Springer-Verlag).
- Klein, R. I., McKee, C. F., & Colella, P. (1994), *Astrophys. J.*, **420**, 213.
- Klein, R. I. (1999), *J. Comp. App. Math.*, **109**, 123.
- Krumholz, M. R., Klein, R. I., & McKee, C. F. (2007a), *Astrophys. J.*, **665**, 478.
- Krumholz, M. R., Klein, R. I., & McKee, C. F. (2007b), *Astrophys. J.*, **667**, 626.
- Krumholz, M. R., McKee, C. F., & Klein, R. I. (2004), *Astrophys. J.*, **611**, 399.
- (2005), *Astrophys. J. Lett.*, **618**, L33.
- Levermore, C. D. (1984), *J. Quant. Spectr. Rad. Trans.*, **31**, 149.
- Levermore, C. D. & Pomraning, G. C. (1981), *Astrophys. J.*, **248**, 321.
- Londrillo, P., & Del Zanna, L., (2004) *J. Comp. Phys.*, 195, 17
- Lowrie, R. B. & Morel, J. E. (2001), *J. Quant. Spectr. Rad. Trans.*, **69**, 475.
- Lowrie, R. B., Morel, J. E., & Hittinger, J. A. (1999), *astrophys. J.*, **521**, 432.
- Mignone, A., Bodo, G., Massaglia, S., Matsakos, T., Tesileanu, O., Zanni, C., & Ferrari, A., 2007, astro-ph/070185
- Mihalas, D. & Auer, L. H. (2001), *J. Quant. Spectr. Rad. Trans.*, **71**, 61.
- Mihalas, D. & Klein, R. I. (1982), *Journ. Comp. Phys.*, **46**, 97.
- Mihalas, D. & Weibel-Mihalas, B. (1999), *Foundations of Radiation Hydrodynamics* (Mineola, New York: Dover).
- Miniati, F. & Colella, P. (2006), *Journ. Comp. Phys.*, submitted, astro-ph/0601519.

- Miyoshi, T. & Kusano, K., (2005) *J. Comp. Phys.*, **208**, 315.
- Pember, R. B. (1993), *SIAM Journal on Scientific Computing*, **14**, 824.
- Pen, U.-L., Arras, P., & Wong, S., (2003) *Ap.J.Supp.*, 149, 447
- Pomraning, G. C. (1983), *Astrophys. J.*, **266**, 841.
- Powell, K.G., (1994) *ICASE Report No. 94-24*, Langley, VA
- Powell, K.G., Roe, P.L., Linde, T.J., Gombosi, T.I., & de Zeeuw, D.L., (1999) *J. Comp. Phys.*, **153**, 284
- Puckett, E. G. & Saltzman, J. S. (1992), *Physica D*, **60**, 84.
- Reinicke, P. & Meyer-ter-Vehn, J. (1991), *Phys. Fluids A*, **3**, 1807.
- Ryu, D., Jones, T.W., & Frank, A., (1995) *Ap.J.*, 452, 785
- Ryu, D., Jones, T.W., (1995) *Ap.J.*, 442, 228
- Ryu, D., Miniati, F., Jones, T.W., & Frank, A., (1998) *Ap.J.*, 509, 244
- Shestakov, A. I. (1999), *Phys. Fluids A*, **11**, 1091.
- Shestakov, A. I. & Greenough, J. A. (2001), AMRH and the High Energy Reinicke Problem, Tech. Rep. UCRL-ID-143937, Lawrence Livermore National Laboratory.
- Shu, F. H. (1992), *Physics of Astrophysics, Vol. II* (University Science Books).
- Stone, J.M., & Norman, M.L., (1992) *Ap. J. Supp.*, 80, 791
- Stone, J.M., Gardiner, T.A., Teuber, P., Hawley, J.F., & Simon, J., 2007, submitted to *Astrophys. J. Supp.*
- Su, B. & Olson, G. L. (1996), *J. Quant. Spectr. Rad. Trans.*, **56**, 337.
- Thompson, T. A., Quataert, E., & Murray, N. (2005), *Astrophys. J.*, **630**, 167.
- Timmes, F. X., Fryxell, B., & Hrbek, G. M. (2006), Spatial-Temporal Convergence Properties of the Tri-Lab Verification Test Suite in 1D for Code Project A, Tech. Rep. LA-UR-06-6444, Los Alamos National Laboratory.
- Toro, E.F., (1999) *Riemann Solvers and Numerical Methods for Fluid Dynamics*, Springer
- Tóth, G., (2002) *J. Comp. Phys.*, 161, 605
- Tóth, G., & Roe, P. (2002) *J. Comp. Phys.*, 180, 736
- Truelove, J. K., Klein, R. I., McKee, C. F., Holliman, J. H., Howell, L. H., & Greenough, J. A. (1997), *Astrophys. J. Lett.*, **489**, L179.
- Truelove, J. K., Klein, R. I., McKee, C. F., Holliman, J. H., Howell, L. H., Greenough, J. A., & Woods, D. T. (1998), *Astrophys. J.*, **495**, 821.
- Turner, N. J. & Stone, J. M. (2001), *Astrophys. J. Supp.*, **135**, 95.
- Turner, N. J., Stone, J. M., Krolik, J. H., & Sano, T. (2003), *ApJ*, **593**, 992.
- Whitehouse, S. C. & Bate, M. R. (2004), *Mon. Not. Roy. Ast. Soc.*, **353**, 1078.
- Whitehouse, S. C., Bate, M. R., & Monaghan, J. J. (2005), *Mon. Not. Roy. Ast. Soc.*, **364**, 1367.
- Zachary, A.L., Malagoli, A., & Colella, P., (1994) *SIAM J. Sci. Comput.*, 15, 263
- Ziegler, U., (2005) *A&A*, 435, 385